SANDIA REPORT

SAND2016-0065
Unlimited Release
Printed January 2016

Extended-Term Dynamic Simulations with High Penetrations of Photovoltaic Generation

Ricky Concepcion, Matt Donnelly, Ryan Elliott, Juan Sanchez-Gasca

Prepared by
Sandia National Laboratories
Albuquerque, New Mexico 87185 and Livermore, California 94550

Sandia National Laboratories is a multi-program laboratory managed and operated by Sandia Corporation, a wholly owned subsidiary of Lockheed Martin Corporation, for the U.S. Department of Energy's National Nuclear Security Administration under contract DE-AC04-94AL85000.

Sandia National Laboratories

Issued by Sandia National Laboratories, operated for the United States Department of Energy by Sandia Corporation.

Available to DOE and DOE contractors from
U.S. Department of Energy
Office of Scientific and Technical Information
P.O. Box 62
Oak Ridge, TN 37831

Telephone: (865) 576-8401
Facsimile: (865) 576-5728
E-Mail: reports@adonis.osti.gov
Online ordering: http://www.osti.gov/bridge

Available to the public from
U.S. Department of Commerce
National Technical Information Service
5285 Port Royal Rd
Springfield, VA 22161

Telephone: (800) 553-6847
Facsimile: (703) 605-6900
E-Mail: orders@ntis.fedworld.gov
Online ordering: http://www.ntis.gov/help/ordermethods.asp?loc=7-4-0#online

SAND2016-0065
Unlimited Release
Printed January 2016

Extended-Term Dynamic Simulations with High Penetrations of Photovoltaic Generation

Ricky Concepcion and Ryan Elliott
Electric Power Systems Research
Sandia National Laboratories
P.O. Box 5800
Albuquerque, NM 87185-1140

Matt Donnelly
Electrical Engineering
Montana Tech
Butte, MT 59701

Juan Sanchez-Gasca
GE Energy
Schenectady, NY 12345

Abstract

The uncontrolled intermittent availability of renewable energy sources makes integration of such devices into today's grid a challenge. Thus, it is imperative that dynamic simulation tools used to analyze power system performance are able to support systems with high amounts of photovoltaic (PV) generation. Additionally, simulation durations expanding beyond minutes into hours must be supported. This report aims to identify the path forward for dynamic simulation tools to accommodate these needs by characterizing the properties of power systems (with high PV penetration), analyzing how these properties affect dynamic simulation software, and offering solutions for potential problems. We present a study of fixed time step, explicit numerical integration schemes that may be more suitable for these goals, based on identified requirements for simulating high PV penetration systems. We also present the alternative of variable time step integration. To help determine the characteristics of systems with high PV generation, we performed small signal stability studies and time domain simulations of two representative systems. Along with feedback from stakeholders and vendors, we identify the current gaps in power system modeling including

fast and slow dynamics and propose a new simulation framework to improve our ability to model and simulate longer-term dynamics.

Acknowledgment

This research was supported by the U.S. Department of Energy, SunShot Initiative, under Agreement No. 29095. Sandia National Laboratories is a multi-program laboratory managed and operated by Sandia Corporation, a wholly owned subsidiary of Lockheed Martin Corporation, for the U.S. Department of Energy's National Nuclear Security Administration under contract DE-AC04-94AL85000.

This page intentionally left blank.

Contents

List of Figures

List of Tables

Executive Summary

This project aimed to identify the path forward for dynamic simulation tools to accommodate these needs by characterizing the properties of power systems (with high PV penetration), analyzing how these properties affect dynamic simulation software, and offering solutions for potential problems.

We focused on improving the feasibility of extended-term dynamic simulations of power systems with very high PV penetration primarily from the perspective of numerical integration. We saw that moving into the extended-term regime presented issues such as increased computational burden and data storage use and proposed modifying how simulation software performs numerical integration in order to address these concerns. Since some of the most commonly used power system simulation software make use of the explicit second order Adams-Bashforth integration method, we investigated other explicit integration methods due to their relative ease of implementation.

Since numerical stability is a primary concern for numerical integration, we analyzed the dynamic stability properties of power systems with increased PV penetration. We identified how different power system dynamic models affect system modes and what role they play in selecting an integrator. Based on our investigations, we found that while increased PV penetration does have an effect on system dynamic behavior, it is rarely a primary factor in stressing the selection of an integrator. We found that the presence of certain components, such as induction motor loads, is most often the driving force in integrator and step size selection.

We found that the fourth order Crane-Klopfenstein predictor-corrector scheme to be a viable numerical integrator because its region of absolute stability shape encompasses the entirety of typical power system eigenvalues even at increased step sizes. This potential increase in step size can produce a lot of computational and storage savings for extended-term simulations. On the other hand, in terms of numerical stability, we found that this scheme is incompatible with high frequency, fast decaying modes associated with induction motor loads. In such cases, we found that Heun's method is similarly accommodating for system eigenvalues at a given step size and is a safe alternative when the system's dynamic characteristics are unknown or problematic for CK-4.

We studied two systems, the Kline-Rogers-Kundur and miniWECC systems, using eigenvalue analysis and time domain simulations. We identified and verified the dominant modes from eigenvalue analysis using spectral estimation techniques on transient simulation results at increasing PV penetration levels. We found that while there is no definitive trend of mode damping with increased PV penetration, system eigenvalues were likely to drift left in the s-plane, which may become a factor in numerical stability. Additionally, we observed issues associated with reduced system inertia through generation drop simulations, such as lower frequency nadirs, slower recovery, and lower settling frequency.

We identified a need to improve system dynamics modeling, especially for slower and faster dynamics (such as AGC and PLL, respectively) and proposed a simulation framework to improve our capabilities to model high PV penetration scenarios.

Nomenclature

AB-2 second order Adams-Bashforth integration method

CK-4 fourth order Crane-Klopfenstein integration method

KRK Kline-Rogers-Kundur

PSLF Positive Sequence Load Flow

PSS/E Power Transmission System Planning Software

PST Power Systems Toolbox

PV photovoltaic

Chapter 1

Introduction

In the quest for a clean and sustainable future, there exists a large push towards incorporating substantial amounts of renewable energy sources such as photovoltaic (PV) generation. The uncontrolled intermittent availability of renewable energy sources makes integration of such devices into today's grid very challenging. Technical issues include energy and power balancing, voltage regulation and stability, frequency regulation, transient stability, and small-signal stability. Another challenge is that the characteristics of a grid with high PV penetration, e.g. 100% of load, will have dynamics significantly different from the grid of today. Currently, transient simulations capture the electro-mechanical response of the grid to various disturbances. A grid dominated by inertia-less generation (e.g. renewables with inverters) will potentially be more responsive to disturbances.

The topic of extended-term time-domain simulation for electric power systems is beginning to garner increasing attention in the literature. In [11], the authors proposed an integration method called Hammer-Hollingsworth 4 (HH-4), which is a special case of the implicit fourth order Runge-Kutta method that is A-stable, possesses the same stability domain as the trapezoidal rule (2nd-order Adams-Moulton method), and has a higher order of accuracy than the trapezoidal rule [10].

A numerical method is said to be A-stable if all of its solutions to equations of the form:

$$\frac{\mathrm{d}}{\mathrm{d}t}y = ky, k \in \mathbb{C} \tag{1.0.1}$$

$$y(t) = Ae^{kt} \; \forall \; \mathrm{Re}(k) < 0 \tag{1.0.2}$$

decay to zero as $t \to \infty$ [6]. This means that for differential equations for which the true solution decays to zero as a function of time, the numerical solution also decays, rather than diverging. Equivalently, a method is A-stable if its region of stability contains all of the left half-plane [6]:

$$\text{Region of Stability} \supseteq \{h\lambda \in \mathbb{C} | \mathrm{Re}(h\lambda) < 0\} \tag{1.0.3}$$

where h represents the simulation step size and λ represents the continuous-time system eigenvalues.

Because the HH-4 method is implicit, the state update equations constitute a nonlinear system which must be solved iteratively. This makes the method much more computationally intensive than linear multistep methods and predictor-corrector schemes and dependent on the specific set of differential equations. Additionally, all fourth order Runge-Kutta methods including HH-4, require the calculation of the state derivatives to be performed four times per integration step. In

contrast, a predictor-corrector scheme based on the trapezoidal rule requires the state derivatives to be calculated only twice. The region of stability of the trapezoidal rule is ideal because it includes all of the left half of the complex plane, and none of the right. However, the trapezoidal rule is also an implicit method, which makes it nontrivial to implement in software in addition to its computational challenges. The integration techniques collectively called predictor-corrector methods serve as a compromise in which the solution to an implicit method is approximated using purely explicit formulations [13].

At present, the standard commercial tools for performing time-domain simulation of large-scale power systems employ explicit, multistep numerical integration methods with a fixed step size. The integrator employed by PSLF and PSS/E, the second order Adams-Bashforth method (AB-2), has a region of stability that is a subset of the left half of the complex plane. This means that the currently employed numerical integration schemes have the potential to exhibit numerical instability for stable systems [2].

An ideal numerical integration scheme for dynamic simulation purposes would possess a larger region of stability and a higher order of accuracy than AB-2. An intelligently chosen predictor-corrector scheme could satisfy both criteria. Since predictor-corrector schemes are explicit formulations, they cannot be A-stable like the trapezoidal rule [30]. However, they can possess a significantly larger region of stability than AB-2, allowing for larger simulation step sizes [23].

The practical implication of this is that the choice of step size for an explicit integration scheme will impact whether or not it exhibits numerical instability. However, numerical stability cannot be the only consideration for integrator selection. There is an inherent trade-off between numerical accuracy and computational workload when the step size of a simulation is modified; in general, simulations run faster at the expense of accuracy with larger step sizes. For explicit methods, the step size must be tuned appropriately such that the eigenvalues of the system reside within the region of stability. Therefore, it is essential to understand the eigenvalue topology of typical power system models, possibly with very high PV penetration, in order to make the best compromise on numerical integrator selection that makes extended-term simulations viable.

The goal of this study was to develop a path forward for dynamic simulation tools that enable analysis of power system performance (with high PV penetration) for a period of minutes to hours. The uncontrolled intermittent availability of renewable energy sources makes integration of such devices into today's grid very challenging. This effort looked at the fundamental drivers, the algebraic and differential equations that model a grid with 100% PV generation, to identify the path forward for dynamic simulation tools that support high renewables as well as longer simulation times which are required to better characterize the impact of renewable variability on dynamic performance.

Chapter 2

Characteristics and requirements for large-scale simulations with high PV penetrations

In stability studies, the dynamic behavior of a power system can be fully described by a set of algebraic equations that is a coupled to a system of differential equations [23]. The characteristics of the algebraic and differential equations required to accurately simulate systems with high PV penetrations stem from augmentations of traditional dynamic simulation formulations. The two basic sets of equations that constitute the simulation framework have the following form [24]:

$$\text{(differential)} \qquad f(x,v) = x' \tag{2.0.1}$$

$$\text{(algebraic)} \qquad g(x,v) = Yv - i(x,v) = 0 \tag{2.0.2}$$

where:

$x \triangleq m \times 1$	vector of state variables
$x' \triangleq m \times 1$	vector of state variable derivatives with respect to time
$v \triangleq n \times 1$	vector of complex bus voltages
$Y \triangleq n \times n$	network admittance matrix
$i \triangleq n \times 1$	vector of complex current injections at each bus

In practice, the vast majority of inverter-coupled renewable generation is supplied by voltage-source converters (VSCs) [7]. Voltage-source converters are high-bandwidth current regulators [7]. At a high level, the objective of inverter control schemes is to regulate current to maintain desired real and reactive power output levels. In the set of algebraic equations, the current injections from PV inverters are accounted for using the same physical description as constant current loads. For VSCs the real power "load" is negative, indicating a net injection into the grid. In the equations below, the P_i and Q_i terms indicate the constant current components of the injection.

$$P = P_p + P_i|v| + P_y|v|^2 \tag{2.0.3}$$
$$Q = Q_p + Q_i|v| + Q_y|v|^2 \tag{2.0.4}$$

The algebraic and differential equations that describe the dynamic behavior of a power system are coupled together and must be solved at each time step. This coupling can be seen more clearly by expressing the two sets of equations in a slightly different way:

$$Ey' = w(y) \tag{2.0.5}$$

where:

$$y \triangleq \begin{bmatrix} x \\ v \end{bmatrix} \tag{2.0.6}$$
$$w \triangleq \begin{bmatrix} f \\ g \end{bmatrix} \tag{2.0.7}$$
$$E \triangleq \begin{bmatrix} I & 0 \\ 0 & 0 \end{bmatrix}, \quad I \triangleq m \times m \text{ identity matrix} \tag{2.0.8}$$

This yields a single set of equations, the total number of which is equal to the sum of the number of state variables plus the number of buses in the system.

2.1 Simulation software prototyping and modeling PV generation

After careful consideration, we selected Power Systems Toolbox (PST) for MATLAB as the simulation environment for this project [4]. This decision was based on project team members' existing experience with the software in addition to its long track record of providing value to the R&D community. PST was originally conceived by Dr. Joe Chow at Rensselaer Polytechnic Institute (RPI) and later upgraded and maintained by Dr. Graham Rogers at Cherry Tree Scientific Software. It was designed to enable scientists and engineers in the research community to perform power flow and dynamic analysis directly in MATLAB, without having to resort to commercial software tools that are both computationally and financially expensive. PST has the benefit of being open source, and completely modifiable. This means that the platform enables researchers to implement custom numerical integration algorithms, which is of course impossible in environments like PSLF and PSS/E.

Dr. Trudnowski at Montana Tech uses PST extensively for modal analysis of the Western Interconnection using a reduced order model of the system (the "miniWECC") [28]. This model was invaluable in this project as a relatively larger test case which could be validated against

existing research using both the mini WECC and more complete representations of the Western Interconnection. Additionally, Dr. Trudnowski aided the project team by providing a modified version of PST that includes the ability to model arbitrary power or current injections into a bus. We used this utility to model PV generation as constant current injections [28].

We described increases in PV penetration by creating a parameter that we called the "solar fraction." This continuous, fraction-valued parameter is used to shift power generation from synchronous machine sources with inertia to inertialess sources modeled as current injections — our implementation of PV generation. In order to model the relative decrease in reactive power output by PV generation, we reduced the amount of reactive power produced by an aggregate of sources as solar fraction values increased. In this project, we used a 50% reduction. For example, suppose that representative plant A in a system model is slated to produce 7.00 p.u. active power and 1.61 p.u. reactive power when all of its constituent units are synchronous machines. If we declare that this system has 50% PV, then the machine representing synchronous generation at plant A will produce 3.50 p.u. active power and 0.805 p.u. reactive power. Meanwhile, the device representing PV generation at plant A will also produce 3.50 p.u. active power but only 0.4025 p.u. reactive power. Additionally, the mVA base of the machine at plant A is reduced by 50% to model the reduction of inertia as generation shifts to an inertialess source. In short, PV% throughout the analysis in this report refers to the solar fraction value used in each simulation; essentially, it is a parameter that relates to total system generation rather than system load.

This page intentionally left blank.

Chapter 3

Background on linear system stability

Previously, we discussed the stability of a numerical method in the context of A-stability. While A-stability is a property of a numerical method, we would like to discuss numerical stability, which is a property of a specific numerical integrator for a particular dynamical system. Numerical stability, as used in this study, refers to a numerical integration scheme with a particular step size being stable in the same sense as A-stability for a particular system. In other words, if all solutions for a set of differential equations that decay to zero over time also decay to zero using a particular numerical integrator, then that integrator is numerically stable for that system. By extension, an integrator that is numerically stable for one system may not be numerically stable for another system because their eigenvalues may be different.

3.1 Region of absolute stability

This brings up the concept of regions of absolute stability. This property of a numerical integrator allows one to determine if the integrator is numerically stable for a specific system. If all of the eigenvalues of a system reside within the region of absolute stability for a numerical integrator, then the integrator is numerically stable. These regions are subsets of the complex eigenvalue plane and can be computed in a straightforward manner. Refer to the following example.

3.1.1 Example: Region of absolute stability for explicit Forward Euler method

The Forward Euler method is defined using the recurrence relation:

$$y_{n+1} = y_n + hy'_n \tag{3.1.1}$$

where $y'_n = \lambda y$. Now let $w^k = y_{n+k}$ (similar to a z-transform) and let $\bar{h} = h\lambda$. Applying these transformations and substitutions to the recurrence relation yields:

$$w = 1 + h\lambda(1) = 1 + \bar{h} \tag{3.1.2}$$

The resulting expression is called the stability function, a function of $\bar{h}$. The region of absolute stability is the region of the $\bar{h}$-plane for which the magnitude of the roots of the stability function

is less than unity. For this example, the region of absolute stability is:

$$\text{Region of Stability} = \{\bar{h} : |1+\bar{h}| < 1\} \tag{3.1.3}$$

This defines a disk in the $\bar{h}$-plane centered at -1 with a radius of unity.

It is important to note that the region as calculated above is defined in the $\bar{h}$-plane. This means that in order to map it to the complex eigenvalue plane, it must be scaled by $1/h$. Hence, the region of absolute stability size is inversely proportional to simulation step size. This implies that larger step sizes may result in numerical instability; this is also why system stiffness can roughly approximate how small the step size for a simulation needs to be.

To demonstrate the effect of numerical stability on dynamic simulations, we created a test platform in MATLAB. We used a system described by a simple second order differential equation with a complex eigenvalue pair $s = \sigma \pm j\omega$ and simulated the step response of the system. Since the analytical solution is known, we can compare it to the simulated response to illustrate how numerical stability affects simulation quality.

3.1.2 Example: 2nd order ODE

Case 1: System eigenvalues at $s = -1 \pm j2$ The system eigenvalues are well within the region of absolute stability for the integrator. The simulated response slightly deviates from the analytical solution but converges correctly.

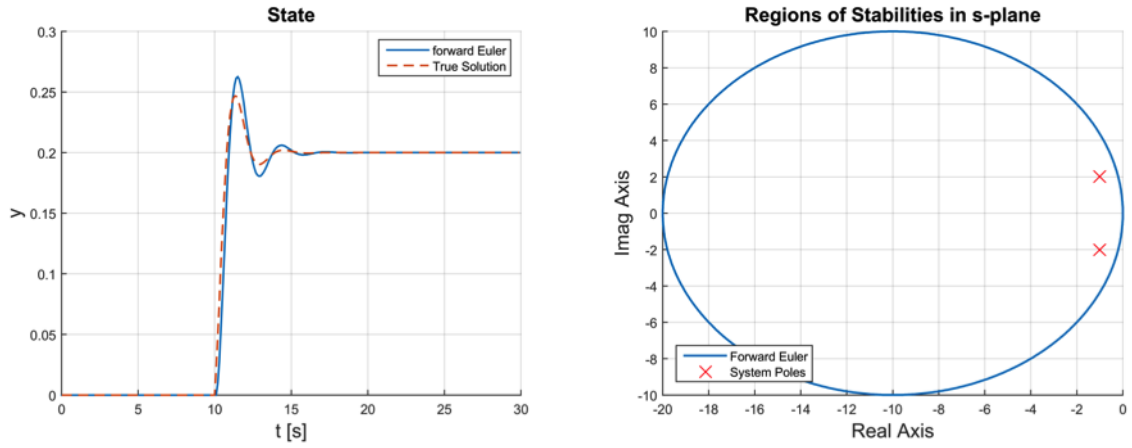

Figure 3.1. This integrator is numerically stable for this system.

Case 2: System eigenvalues at $s = -0.5 \pm j2$ The system eigenvalues are encroaching upon the region boundary from within. The simulated response is stable but not accurate — it exhibits numerical oscillations.

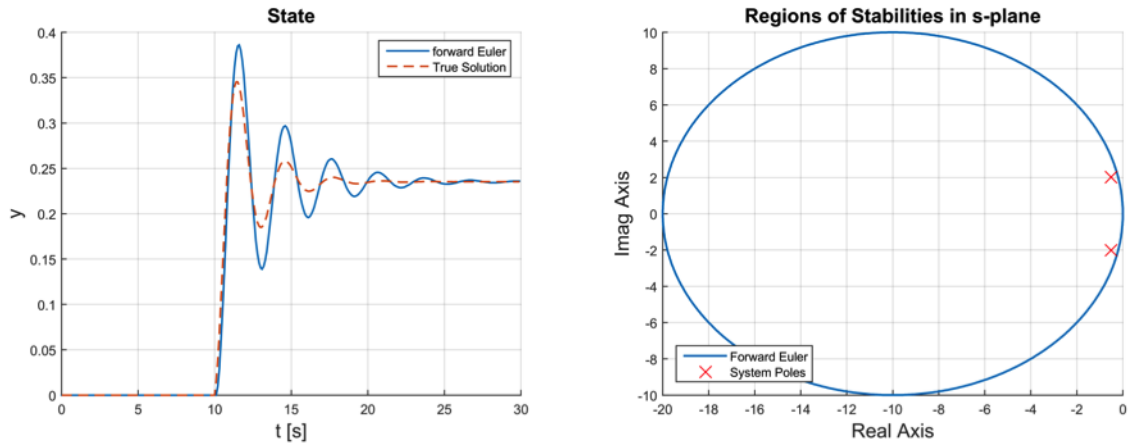

Figure 3.2. This integrator is numerically stable for this system but suffers from numerical oscillations.

Case 3: System eigenvalues at $s = -0.1 \pm j2$ The system eigenvalues are outside the region of absolute stability. The simulated response is unstable and inaccurate — the analytical solution is stable but the simulated response diverges. The simulation is not only inaccurate but qualitatively incorrect.

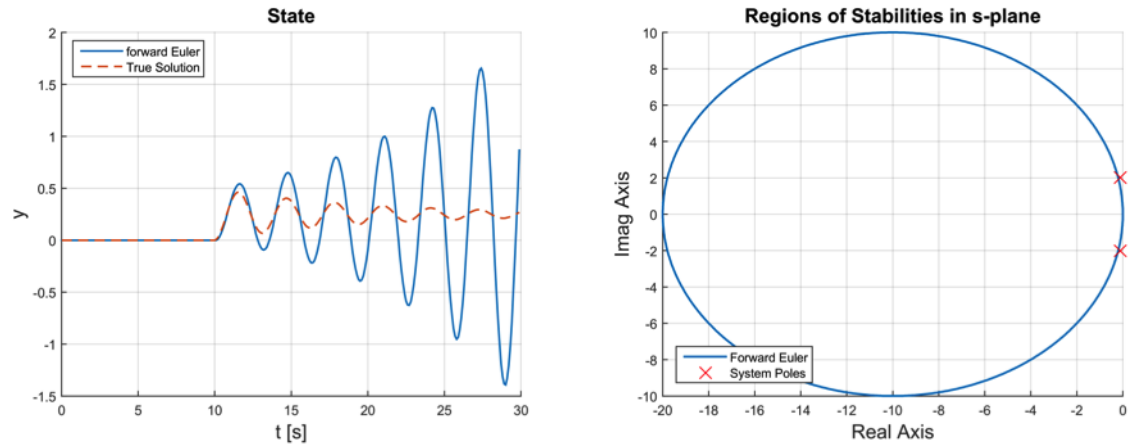

Figure 3.3. This integrator is numerically unstable..

The takeaway here is that for a given numerical method, it is essential that the numerical integrator be stable. Furthermore, depending on preference, it is important to keep in mind that

numerical oscillations will occur if system eigenvalues are stable but near the boundary of the region of absolute stability.

In this study, we sought to propose suitable integration schemes for dynamic simulation over long time periods. One method of increasing extended-term simulation viability is to increase the step size of the integrator. As we have demonstrated, we are limited in this regard by numerical stability. For implicit methods, numerical stability is not much of a concern as A-stability is a possibility whereas it is not for explicit methods. However, implicit methods tend to be relatively difficult to implement and computationally expensive. For improved accuracy, we would also like to consider higher order numerical methods but likewise they come at the cost of increased computation and memory needs.

3.2 Stiffness overview

One of the hypotheses of this study was that system stiffness would increase with PV penetration. System stiffness is a property of the set of differential equations that describe the dynamics of the system. To measure system stiffness, we used the stiffness ratio:

$$\text{stiffness ratio} = \frac{\max|\text{Re}(\lambda)|}{\min|\text{Re}(\lambda)|} \tag{3.2.1}$$

This property of a system of differential equations roughly describes the range of dynamics present in the system; a large stiffness ratio implies that there are modes with very fast decay rates, very slow decay rates, or a combination of both. Intuitively, this represents a type of difficulty in integrating the associated differential equations; both fast and slow dynamics need to be accounted for. However, the simplicity of this quantity implies that it may not be sufficient to wholly describe a system's characteristics with respect to numerical integration.

In order to analyze the stiffness of power systems, we used PST's linearization capabilities. Tools included with PST for small signal stability studies enable users to estimate properties of power system test cases such as system eigenvalues and associated left and right eigenvectors. In the next section, we study two representative power system models and examine how system stiffness impacts numerical integrator selection.

Chapter 4

Stiffness analysis

In this section, we examine the system eigenvalues and stiffness of a small, 13-bus test case, the Kline-Rogers-Kundur (KRK) system as well as a larger test case, the miniWECC.

4.1 Kline-Rogers-Kundur (KRK) system

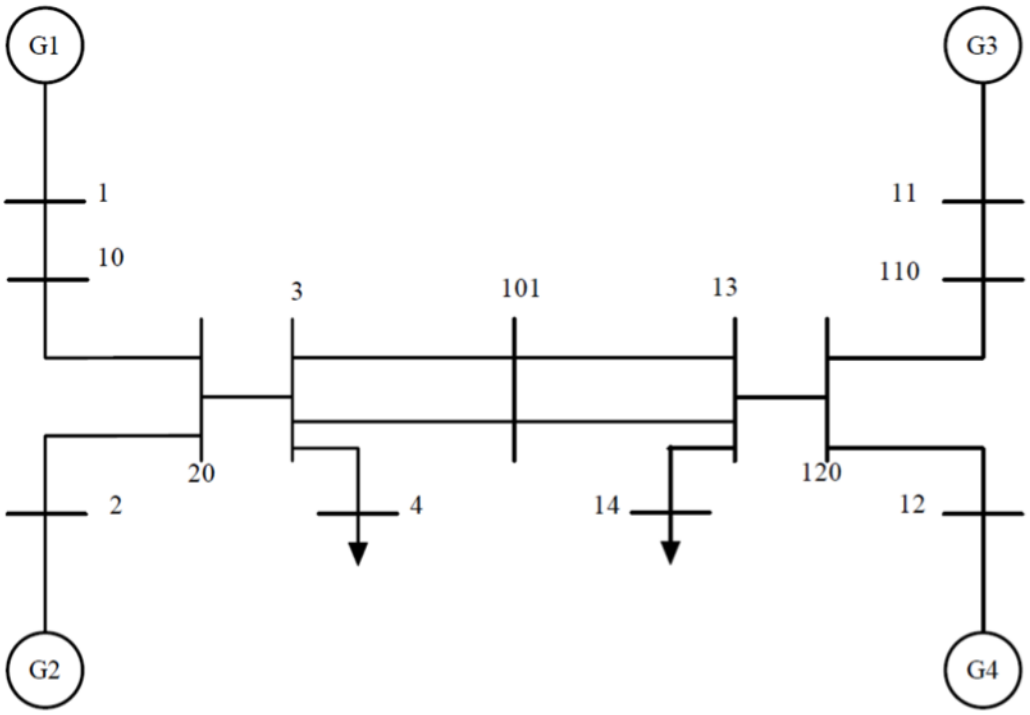

Figure 4.1. The Kline-Rogers-Kundur system one line diagram.

This test system [15] was created to study interarea and local modes using a small, simple, but realistic setup. It was included with PST in a variety of flavors. We modified a version of it that was loaded with subtransient machine models, IEEE type DC1 excitation systems, and simplified

turbine/governor models. We added PV generation to this system that varied depending on the study.

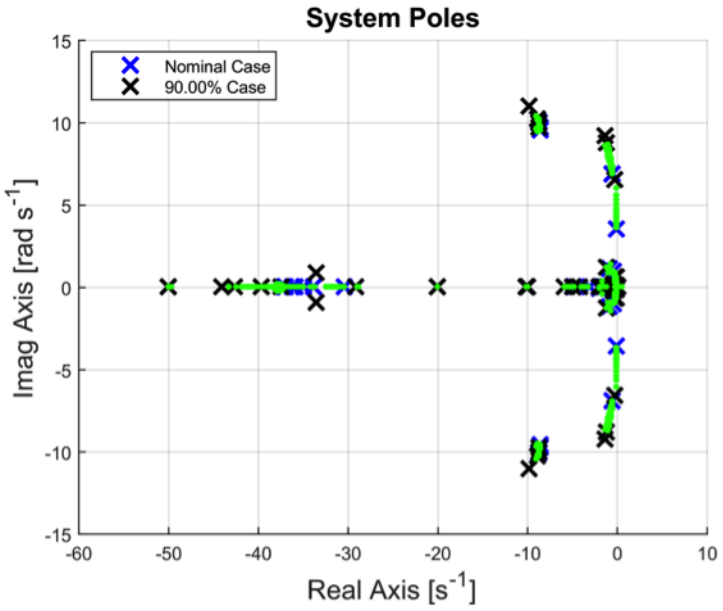

Figure 4.2. System eigenvalue sweep map.

In the following eigenvalue sweep diagrams, the system eigenvalues are plotted in the complex s-plane. As we will observe, this arrangement of system eigenvalues seems to be prototypical for the test cases encountered thus far. Typically, the relatively higher frequency eigenvalue pairs in the 0.8-1.6 Hz range have larger time constants and tend to aggregate near the $j\omega$-axis. The largest magnitude eigenvalues in most cases tend to be purely real. Upon further investigation, the location of the largest magnitude eigenvalues is directly governed by the smallest time constant in the system, which tends to be part of the exciter dynamics.

It was hypothesized that increased solar penetration levels would increase system stiffness. As we have shown, this is definitively not the case. Empirically, we cannot conclude that an increase in solar penetration levels definitely increases the stiffness of the system. In this system, we observe the opposite: increasing solar penetration decreases system stiffness. This can be explained by the fact that, since the numerator of the stiffness ratio tends to be invariant with respect to solar penetration, the stiffness ratio is entirely governed by (and highly sensitive to) changes in $\min|\mathrm{Re}(\lambda)|$. Anecdotally, we can see massive orders of magnitude differences in stiffness ratio across solar penetration levels due to this sensitivity and eigenvalues sweeping across and around the s-plane origin. In order to mitigate large variations in stiffness ratio that may obscure trends due to hypersensitivity, we only considered eigenvalues with real parts no larger than some threshold when computing $\min|\mathrm{Re}(\lambda)|$.

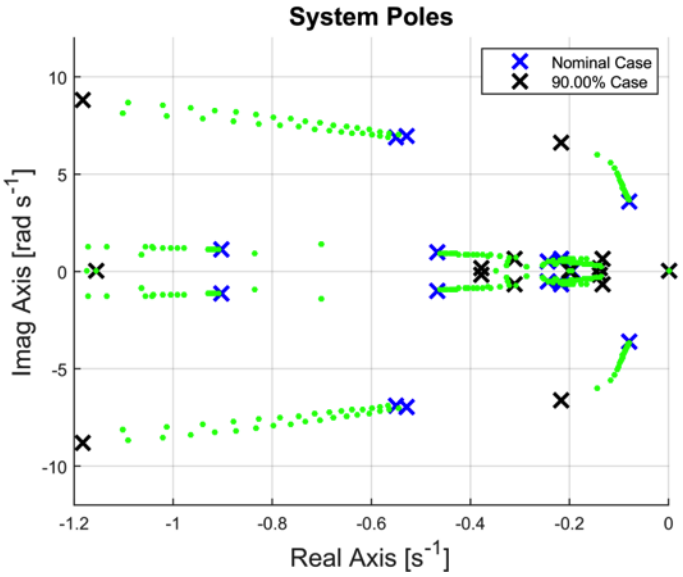

Figure 4.3. Zoom-in of system eigenvalue sweep map, focusing on lightly damped modess.

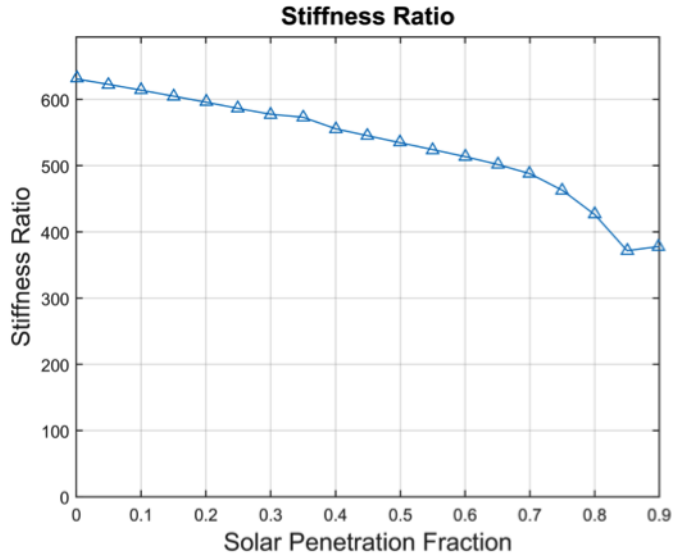

Figure 4.4. Stiffness ratio against PV%.

4.1.1 Selected modes

We used PST's linearization capabilities to try to identify the local and interarea modes of the system. Compass plots were selected to aid in visualizing mode shapes and identifying the types

of modes present in the system. These plots were generated by determining the right eigenvector (mode shape) of the associated with the eigenvalue indicated in the title of each plot. Each entry in these complex-valued vectors correspond to a state in the system; these complex numbers are translated to vectors in the complex plane for the compass plots. Mode shape eigenvectors were normalized such that the largest magnitude component in each eigenvector served as the reference $1 + j0$. Selected state variables, typically machine speeds, were plotted to clearly illustrate state relationships.

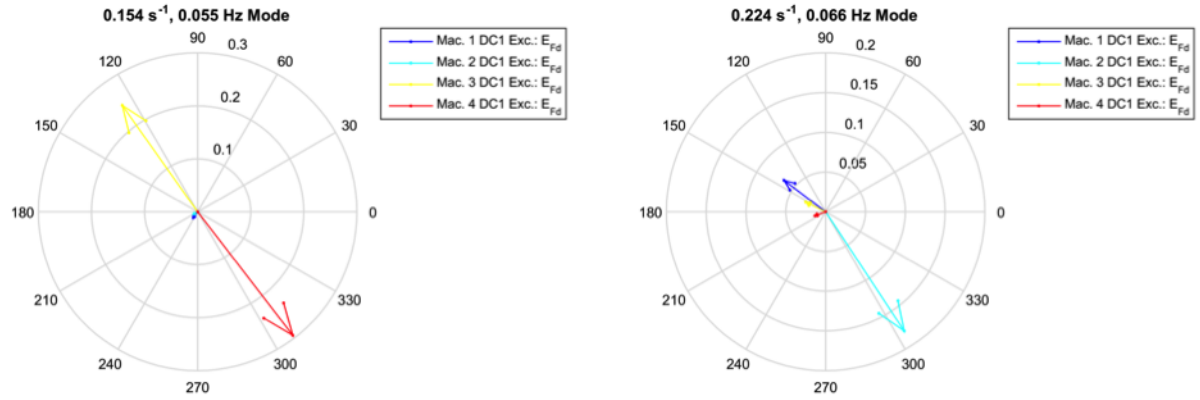

Figure 4.5. Compass plots of local modes of the KRK system base case. (left: area 1, right: area 2)

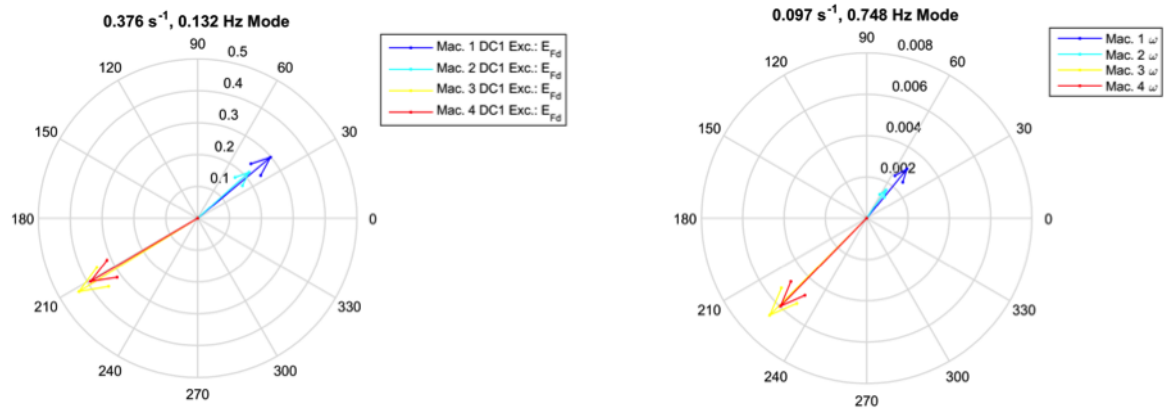

Figure 4.6. Compass plots of interarea modes of the KRK system base case.

In order to characterize the effect of increased PV% on system modes, we tracked the trajectory of the interarea mode as the solar fraction increased. We computed the damping ratio, ξ, based on

the interarea mode eigenvalue at four different solar fraction values. The results are summarized in Table 4.1. We observe that the damping ratio decreases very slightly with increased PV penetration; however, it is difficult to generalize this trend across all systems.

Table 4.1. Damping ratio for different modes in KRK system.

Mode	α [$\mathbf{s}^{(-1)}$]	**f [Hz]**	ξ **[%]**
Interarea (0%)	0.07928	0.5710	2.21%
Interarea (25%)	0.08400	0.6150	2.17%
Interarea (50%)	0.09358	0.7044	2.11%
Interarea (60%)	0.09700	0.7480	2.06%

4.2 Analysis in PSLF

To provide another perspective on our analysis, we recreated the KRK system in PSLF. The intent was to recreate the KRK system with as similar operating conditions and model parameters as the PST case as possible. This comes with the caveat that the dynamic models available in each software platform differ. For example, instead of using the older, IEEE type DC1 exciter models, we used AC4 excitation systems. Most notably, instead of using the simple model for PV generation that we used in PST, we used more sophisticated models for photovoltaic plants that include, for instance, electrical controllers.

Analogously to what was done in the PST studies, we performed a root locus sweep of active power generation. The base case has all power generation in the system coming from synchronous machines. In 20 increments of 35 MW, active power generation is shifted to photovoltaic power plants while reactive power generation is maintained by the synchronous machines. The resulting system eigenvalue map is shown in Figure 4.7.

It is important to note that these results are preliminary as the photovoltaic power plants have not particularly been used to model these types of systems. Focusing on the interarea and local modes, we observe that these modes exhibit an increase in damping as the power generation is shifted to the PV power plants. Contrary to the analysis in PST, these modes primarily increase in damping rather than in frequency; this results in different trends of damping ratio Additionally, even in the base case, we observe that there are higher frequency modes present in the PSLF system compared to the PST system. In particular, the presence of higher frequency with fast decay rates in the PSLF case could prove to be problematic for dynamic simulations with increased step sizes. Nevertheless, we can attribute the appearance of these different modes in the PSLF study to the different dynamic models used, e.g., the electrical controllers.

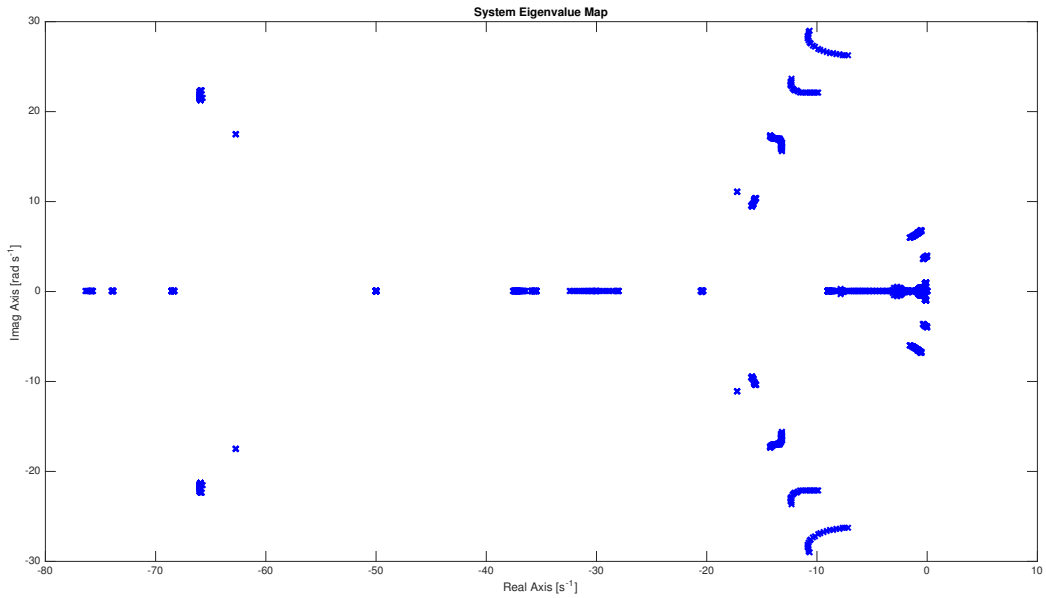

Figure 4.7. PV% sweep of KRK system analog in PSLF.

4.3 miniWECC system

The miniWECC system is a reduced order representation of the western interconnection used for damping control analysis. It consists of 122 buses and 33 machines. Its one line diagram is shown in Figure 4.8. Similarly to the KRK system study, we co-located PV generation with all but one of the conventional generation sources and used the solar fraction parameter to shift generation from the conventional sources to the PV sources while proportionally reducing synchronous machine inertia. The system eigenvalue map resulting from the PV generation sweep is shown in Figure 4.9. A zoomed-in version focusing on lightly damped, oscillatory modes is shown in Figure 4.10. (Note: The PV% only goes up to 70% in these sweeps because larger values estimates the existence of eigenvalues in the right-half plane.)

In the KRK system, we observed a decline in stiffness ratio as the solar fraction increased. In the miniWECC system, we actually observe a static stiffness ratio until it increases at 70% PV (c.f. Figure 4.11). Since the maximum decay rate in the system remains fixed regardless of PV%, this indicates that at least one eigenvalue (pair) is drifting right with increased PV%, causing the increase in stiffness ratio. This is supported by the appearance of unstable modes during a sweep up to 90% PV. Hence, it would be impossible to perform dynamic simulations using this test case as is — the operating point and/or controls would need to be changed/implemented to support high penetrations of PV generation.

The system described by the miniWECC case has been analyzed in the past and has several

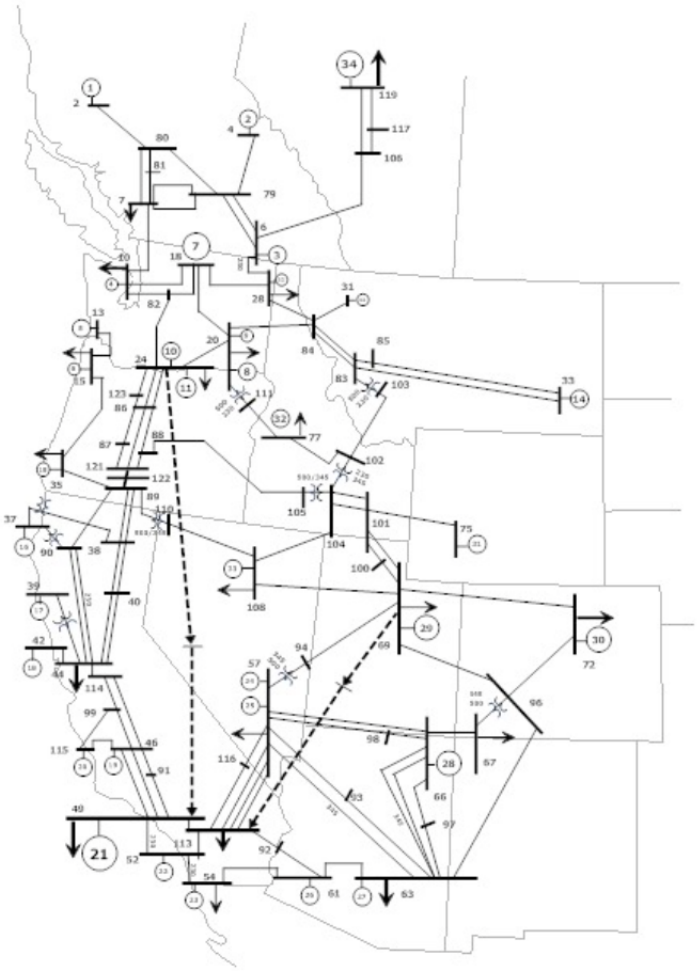

Figure 4.8. The miniWECC system one line diagram, taken from [27].

well-known modes that have been identified and named [27]. We aimed to identify these modes in this section using PST's linearization routine as well as in Section 8 using mode estimation via time domain simulations. The following figures are the compass plots of a selection of these modes at different solar penetration levels. Each vector in the compass plots is the machine speed of the synchronous machine located at the labeled location. The vectors are normalized and referenced in each plot such that the machine speed with the largest participation factor serves as the reference vector $1 + j0$. The remaining vectors displayed are assigned colors depending on their phase relative to the reference vector: the closer to π the vector is, the closer to indigo and further away from red it is (using a "jet" colormap). The state names are based on their geographical locations.

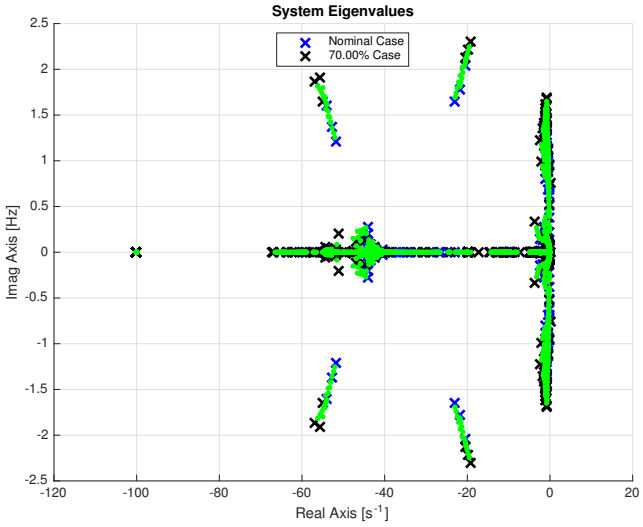

Figure 4.9. System eigenvalue sweep map.

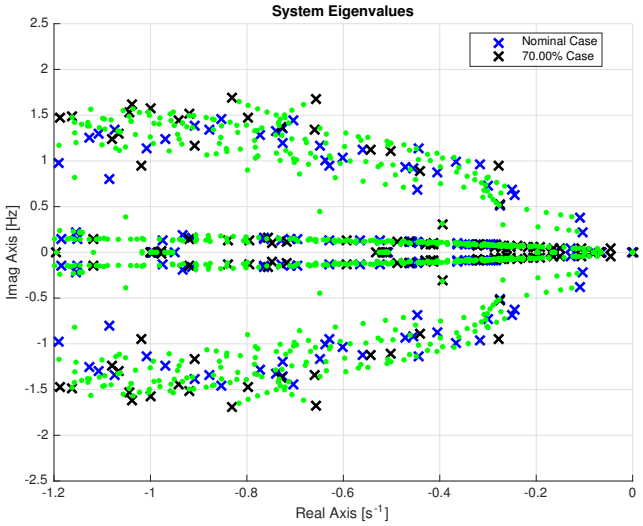

Figure 4.10. Zoom-in of system eigenvalue sweep map, focusing on lightly damped modess.

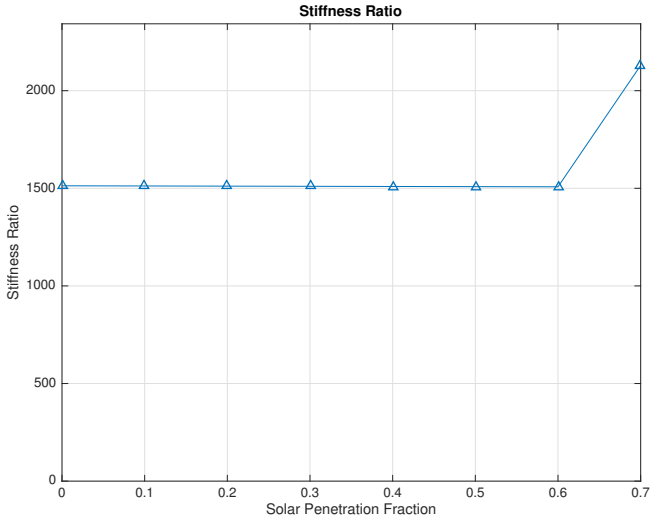

Figure 4.11. Stiffness ratio against PV%.

4.3.1 North-South Mode A

North-South Mode A, nominally at 0.25 Hz, is characterized by the northern half of the miniWECC system swinging against the southern half [27].

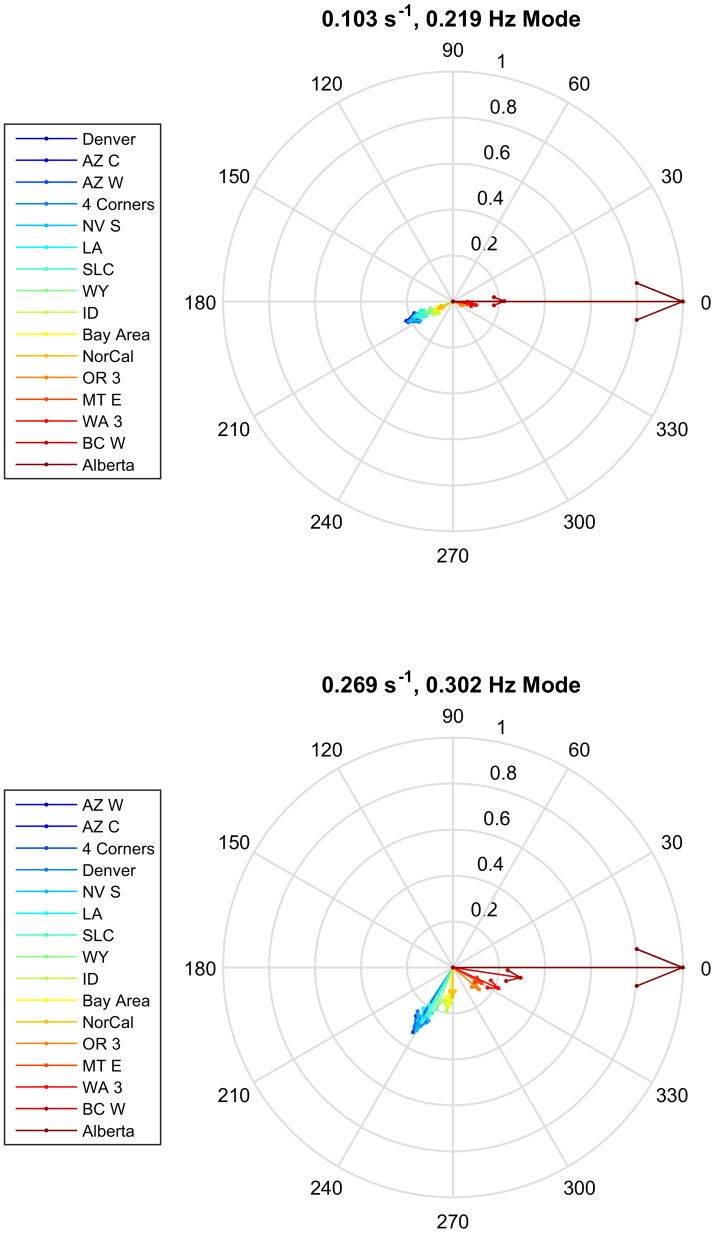

Figure 4.12. North-South Mode A. (top: base case, bottom: 50% PV)

4.3.2 North-South Mode B

North-South Mode B, nominally at 0.4 Hz, is characterized by Alberta swinging against BC and the northern US, which is also swinging against the rest of the system [27].

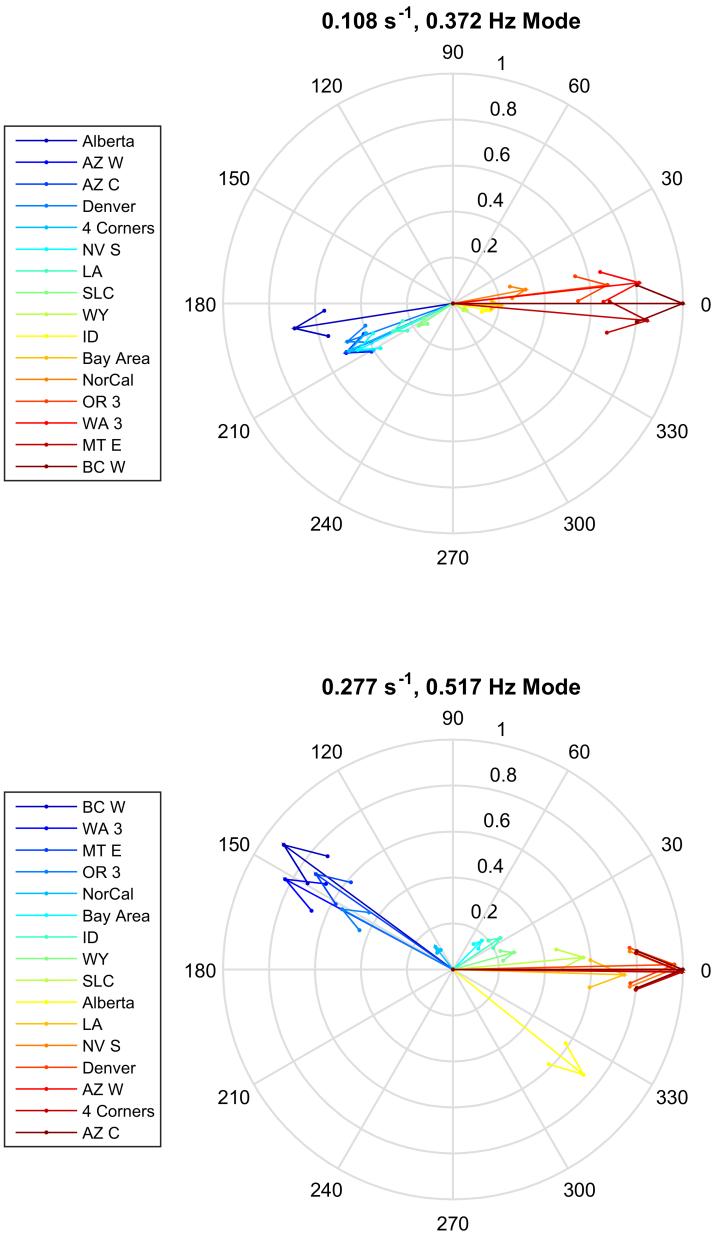

Figure 4.13. North-South Mode B. (top: base case, bottom: 50% PV)

4.3.3 Observations

Using the base case analysis, the frequencies estimated of the North-South modes is in line with what is described in [27], subject to differences in operating conditions. We also tracked the damping ratio of these modes as a function of PV%; the results are shown in Tables 4.2 and 4.3.

Table 4.2. Damping ratios for North-South Mode A in the mini-WECC system.

PV%	α [$s^{(-1)}$]	**f [Hz]**	ξ **[%]**
0%	0.103	0.219	7.5%
25%	0.143	0.250	9.1%
50%	0.269	0.302	14.0%
60%	0.395	0.316	19.5%

Table 4.3. Damping ratios for North-South Mode B in the mini-WECC system.

PV%	α [$s^{(-1)}$]	**f [Hz]**	ξ **[%]**
0%	0.108	0.372	4.6%
25%	0.163	0.423	6.1%
50%	0.277	0.517	8.5%
60%	0.311	0.603	8.2%

The estimated damping ratios for North-South Mode A and B for the base case are in line with the reported ranges of 10-15% and 5-10%, respectively [27]. With increased PV%, the mode shapes of these two modes evolves such that the states become slightly closer in both magnitude and phase. This coincides with the increase in damping ratios of the modes.

4.4 Impact of stiffness on numerical integration scheme selection

For a comprehensive analysis of power system eigenvalues, we used a 16 machine, 68 bus system included with PST. This particular system made use of a subtransient reactance model for its machines, IEEE type 1 DC excitation systems, power system stabilizers, and induction motor loads. Having this variety of dynamic models ensures that we can observe a myriad of eigenvalues that one may have in any given power system model. Furthermore, we augmented the model by adding PV generation to all but one of the generation buses; this allowed us to study how increased PV penetration would affect this variety of eigenvalues.

We used PST's linearization routines to estimate the eigenvalues at discrete levels of solar fraction values, starting from a nominal case of 0% PV up to 90% PV; experimentally, we determined

that either the linearization or power flow would fail beyond 90% PV for this particular case. We then plotted all of the computed eigenvalues simultaneously to illustrate the trajectory of eigenvalues as PV penetration increased. The results are shown in Figure 4.14.

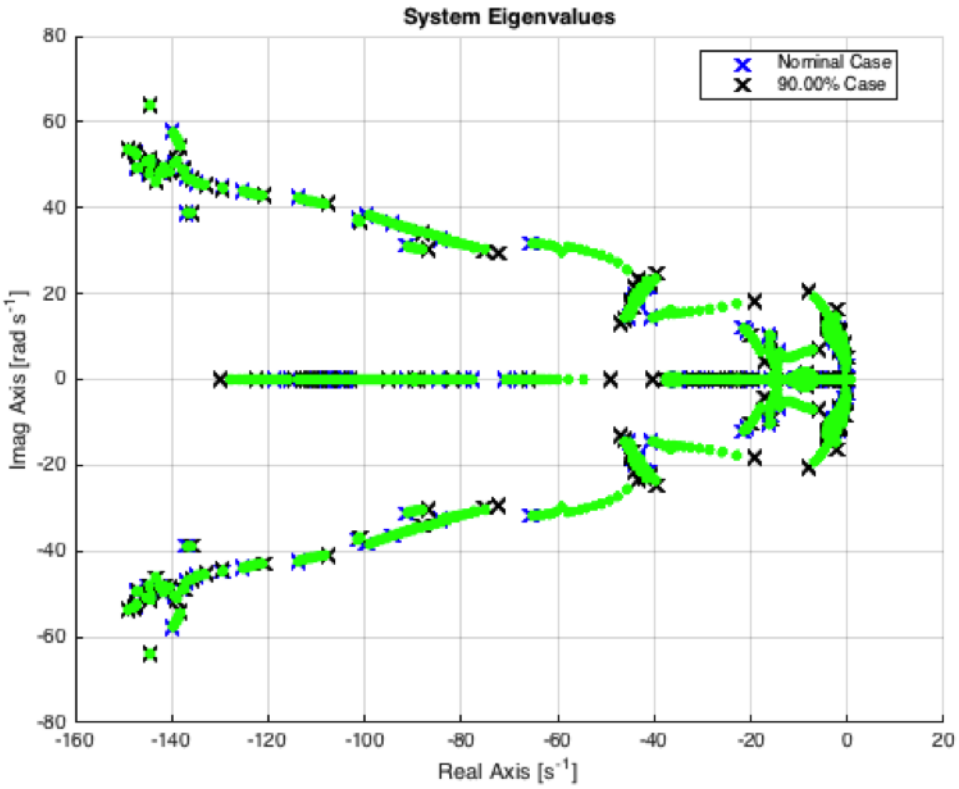

Figure 4.14. System eigenvalue sweep map for 68 bus system.

The estimated eigenvalues constitute a wide variety of frequencies and decay rates. This large range of decay rates would seem to indicate a large stiffness ratio. To confirm, we computed the stiffness ratio across solar fraction values, shown in Figure 4.15.

Notably, there doesn't seem to be any correlation of stiffness ratio with PV generation as hypothesized. To determine why, we plotted min/max decay rate eigenvalues against solar fraction. While the smallest eigenvalue decay rate varied erratically with PV%, the largest eigenvalue decay rate remained fixed (c.f. Figure 4.16) . Throughout the stiffness analysis of other test cases, this trend typically held. The fastest dynamics in these systems tended to be unaffected by PV%. While the slowest dynamics in these systems were affected by PV%, their relationship cannot really be generalized. Therefore, we found it unrealistic to correlate system stiffness (using stiffness ratio) with PV penetration.

While these results on their own are illuminating, we wanted our analysis to be more generalizable, not just specific to this particular test case. We analyzed PST's code to determine the

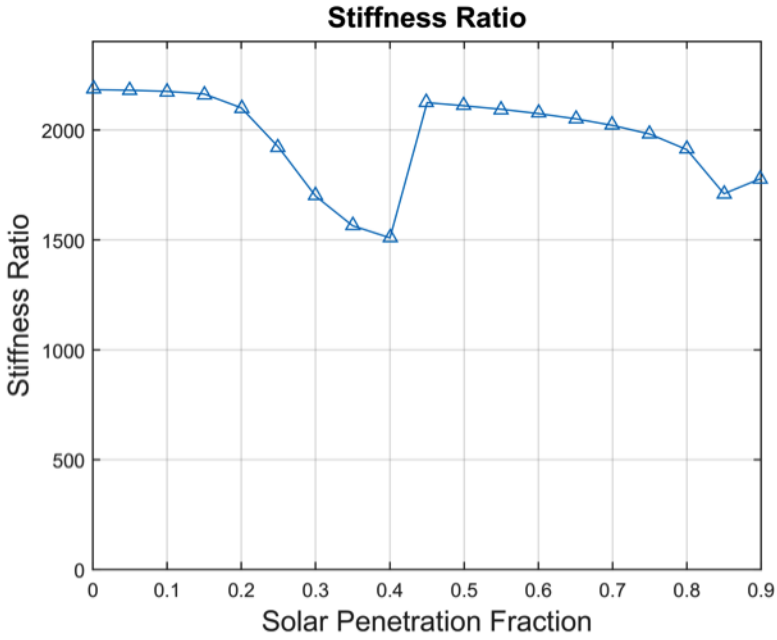

Figure 4.15. Computed stiffness ratio of 68 bus system across different penetration levels.

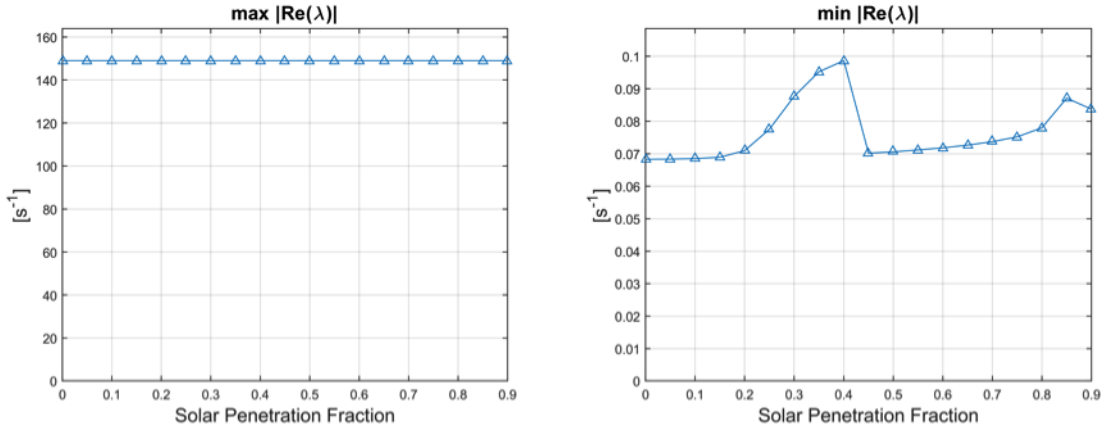

Figure 4.16. Mode decay rates used in stiffness ratio calculations for 68 bus system.

specifics of these eigenvalues. We wanted to know what parts of the power system are responsible for which eigenvalues. With this information, we could predict the arrangement of eigenvalues of any given test case — we called this the "system eigenvalue topology" — based on the dynamic models present in the case specification. In order to do this, we examined the participation factors

of each eigenvalue. The participation factor is defined as:

$$p_{ik} = l_k^i r_k^i \tag{4.4.1}$$

where l^i and r^i are the left and right eigenvectors, respectively, of the ith eigenvalue and k refers to the kth state. An interpretation of the participation factor p_{ik} is the relative participation of the kth state in the ith mode [1]. Hence, a large participation factor implies that that particular state is largely responsible for that particular mode. By relating which state indices mapped to which dynamic model states, we were able to proceed with our analysis.

We studied our 16 machine test case and examined the estimated eigenvalues. We observed that there were definitive regions of the complex eigenvalue plane that would be populated if specific dynamic models were present. The results of our analysis are shown in Figure 4.17.

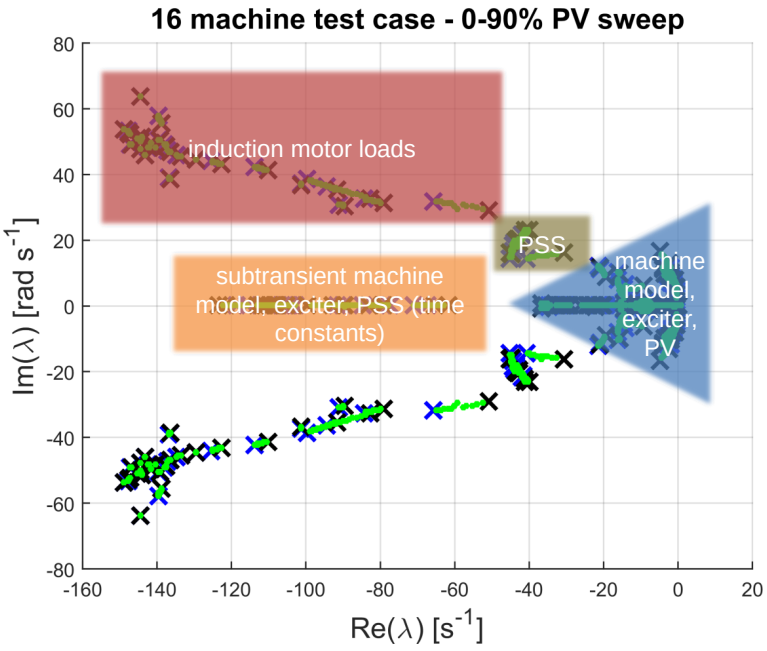

Figure 4.17. System eigenvalue map for 68 bus system with typical eigenvalue locations for common power system model components.

These results are interesting in the context of considering numerical integration methods. Typically, the "simplest" PST test cases consisted of machine models and excitation systems. In these cases, we would not see high frequency modes like those of induction motor loads in the stiffness analysis. Furthermore, the fastest dynamics in the orange region tended to be unaffected by the increasing PV penetration. Therefore, it is unlikely that the requirements for dynamic simulation of systems with high PV penetration would change because of the presence of PV; it is more likely that the presence of certain dynamic models (e.g., induction motor loads) would be the driving

force behind any changes in how these systems are simulated. We will discuss this in more detail when discussing numerical integration methods in the proceeding section.

Chapter 5

Numerical integration scheme analysis

In this study, we sought to propose suitable integration schemes for dynamic simulation over long time periods. One method of increasing extended-term simulation viability is to increase the step size of the integrator. As we have demonstrated, we are limited in this regard by numerical stability. For implicit methods, numerical stability is not much of a concern as A-stability is a possibility whereas it is not for explicit methods. However, implicit methods tend to be relatively difficult to implement and computationally expensive. For improved accuracy, we would also like to consider higher order numerical methods but likewise they come at the cost of increased computation and memory needs.

While we propose that the trapezoidal rule is a suitable choice for the goals of this study, it is difficult to analyze and comes with the aforementioned issues due to being an implicit method. Thus, our focus shifted to viable explicit method candidates, including predictor-corrector methods. In our initial investigations with PST, we learned that the toolbox relies upon a 2nd-order accurate predictor-corrector algorithm known as Heun's method [22]. This integration scheme uses the forward Euler scheme as its predictor and the trapezoidal rule as its corrector. To achieve the goals of this study, we investigated the behavior of the integration scheme employed by PSLF and PSS/E, the two-step Adams-Bashforth method (AB-2). Based on the analysis of system stiffness and other computational requirements, we identified the 4th-order accurate Crane-Klopfenstein (CK-4) predictor-corrector scheme as a candidate explicit integration scheme [5]. The CK-4 integration scheme possesses a high order of accuracy and excellent stability characteristics while being straightforward to implement in software. As a baseline, we included the simple Forward Euler integration scheme although it is not a real candidate due to its limited stability properties and poor accuracy.

The selection of a numerical integration scheme for a dynamical system simulation platform is driven by a number of factors. In particular, there exists a tradeoff chiefly among integrator accuracy, computational and memory burden, ease of implementation, and numerical stability properties. Typically, the first decision when selecting an integration scheme is deciding between using an implicit or explicit scheme. In general, explicit schemes are easier to implement at the cost of accuracy and numerical stability [17] whereas comparable implicit schemes improve in these facets at the cost of ease of implementation and computational burden. For example, a typical explicit integration scheme can be dynamical system agnostic and be written solely in terms of already calculated state derivatives. On the other hand, an implicit integration scheme usually requires solving a set of nonlinear equations which involves significantly more computation. In this

section, we will be comparing four explicit integration schemes:

- Forward Euler method
- Two-step Adams-Bashforth method
- Heun's method
- Four-step Crane-Klopfenstein method

We will examine how the schemes differ in computational burdens both analytically and using experimental benchmarks. We will also be examining accuracy properties in terms of order of accuracy, local truncation error, and accumulated error. Finally, we will look at how the schemes differ in numerical stability using regions of absolute stability. Using these analyses, we will discuss the tradeoff in selecting among these particular schemes in the context of power system simulation.

5.1 Computational considerations

When looking at the computational burden of integration schemes, we primarily look at the number of "rate" calls and number of memory storages and calls per time step or iteration. "Rate" calls are the execution of the routine to compute the derivatives of the state variables in the system. Typically, this is only once per iteration for standard explicit integration schemes but predictor-corrector schemes can include numerous rate calls. Memory access is mostly tied to the order of the integration scheme but can also increase depending on the implementation of a predictor-corrector scheme. We will define each integration scheme to be examined and analyze how each is computationally taxing. Unless explicitly noted, all analysis is done assuming a fixed time step h.

5.1.1 Forward Euler method

The Forward Euler method is a simple first order integration scheme. It is defined as:

$$y_{n+1} = y_n + hf_n \tag{5.1.1}$$

where $f_n = y'_n$ and h is the (fixed) time step. At each iteration of this method, there is a single rate call. There is a single explicit memory call but more may be necessary depending on the state derivative computation. (We will ignore this moving forward because state derivative computation is invariant of the integration scheme of choice.)

5.1.2 Two-step Adams-Bashforth method

The two-step Adams-Bashforth method (AB-2) is a second order integration scheme that is employed by a number of commercial power system simulation software vendors. It is defined as:

$$y_{n+1} = y_n + \frac{h}{2}(3f_n - f_{n-1}) \tag{5.1.2}$$

At each iteration, there is a single rate call. Like the Forward Euler method, there is a single memory call of the current state variable. However, there is also a memory call of a previous time step's state derivative due to AB-2 being a second order method.

5.1.3 Heun's method

Heun's method is the first of the two predictor-corrector methods under consideration. The predictor is a simple Forward Euler step:

$$p_{n+1} = y_n + hf_n(t_n, y_n) \tag{5.1.3}$$

The corrector is a trapezoidal rule step:

$$y_{n+1} = y_n + \frac{h}{2}\left(p'_{n+1} - f_n(t_n, y_n)\right) \tag{5.1.4}$$

where:

$$p'_{n+1} = f(t_{n+1}, p_{n+1}) \tag{5.1.5}$$

is the state derivative computed using the predicted state variable value. This method is sometimes called the explicit trapezoidal rule due to the corrector step. In the predictor step, there is a single memory call (state variable) and a single rate call. With the addition of the corrector step, there are two memory calls (the state variable and the state derivative computed in the predictor step) and an additional rate call to compute the state derivative using the predicted state variable value. This totals three memory calls and two rate calls per iteration.

5.1.4 Four-step Crane-Klopfenstein method

The four-step Crane-Klopfenstein method (CK-4) is a fourth order predictor-corrector method [5]. The predictor is defined as:

$$p_{n+1} = a_2 y_n + b_1 y_{n-1} + c_1 y_{n-2} + d_1 y_{n-3} + h(e_1 f_n + q_1 f_{n-1} + g_1 f_{n-2} + k_1 f_{n-3}) \tag{5.1.6}$$

The corrector is defined as:

$$y_{n+1} = a_2 y_n + b_2 y_{n-1} + c_2 y_{n-2} + h(d_2 p'_{n+1} + e_2 f_n + q_2 f_{n-1} + g_2 f_{n-2}) \tag{5.1.7}$$

The coefficients were numerically computed and are summarized in Table 5.1.

Table 5.1. Four-step Crane-Klopfenstein method coefficients.

$a_1 = 1.547652$	$a_2 = 1$
$b_1 = -1.867503$	$b_2 = 0$
$c_1 = 2.017204$	$c_2 = 0$
$d_1 = -0.697353$	$d_2 = 0.375$
$e_1 = 2.002247$	$e_2 = 0.791666667$
$f_1 = -2.03169$	$f_2 = -0.208333333$
$g_1 = 1.818609$	$g_2 = 0.0416666667$
$k_1 = -0.71432$	

The predictor step requires four memory calls for the state variables, three memory calls for the state derivatives, and one rate call for the current time step state derivative. The corrector step requires three memory calls for the state variables, three memory calls for the state derivatives, and one rate call for the predicted state derivative. This totals 13 memory calls and two rate calls per iteration, a substantial increase over Heun's method. A summary of the rate and memory call counts is shown in Table 5.2.

Table 5.2. Summarizing the number of memory and rate calls for various integration techniques.

	Memory calls	Rate calls
Forward Euler	1	1
AB-2	2	1
Heun's method	3	2
CK-4	13	2

5.1.5 Integrator performance benchmark tests

In order to demonstrate how computational differences among the integrators affect real time performance, we developed a benchmarking tool in MATLAB using our previously mentioned 2nd order ODE test platform. We simulated a step response using each of the integrators of interest. We performed a 100 second simulation for 3 different step sizes; this means that the number of steps in each simulation varied depending on the step size. We simulated 100 different systems in which the eigenvalue pair location each time was randomized but within the region of absolute stability for all integrators. The simulations were performed on a laptop computer with an Intel Core i7-4600U CPU 2.1 GHz and 8.00 GB of RAM running Windows 7. The results, in seconds, are shown in Table 5.3.

In order to see how average simulation time scaled with step size/step count, we did a similar experiment with a broader range of step sizes. The results are shown in Figure 5.1.

Table 5.3. Total time taken to complete 100 simulations for various step sizes.

Total Time [s]			
	$h = \frac{1}{4}$ **cycle**	$h = \frac{1}{2}$ **cycle**	$h = 1$ **cycle**
Forward Euler	19.50729	9.320980	4.744207
AB-2	22.70859	10.77197	5.325676
Heun's method	33.04143	15.54170	7.731683
CK-4	50.57874	23.36001	11.599648

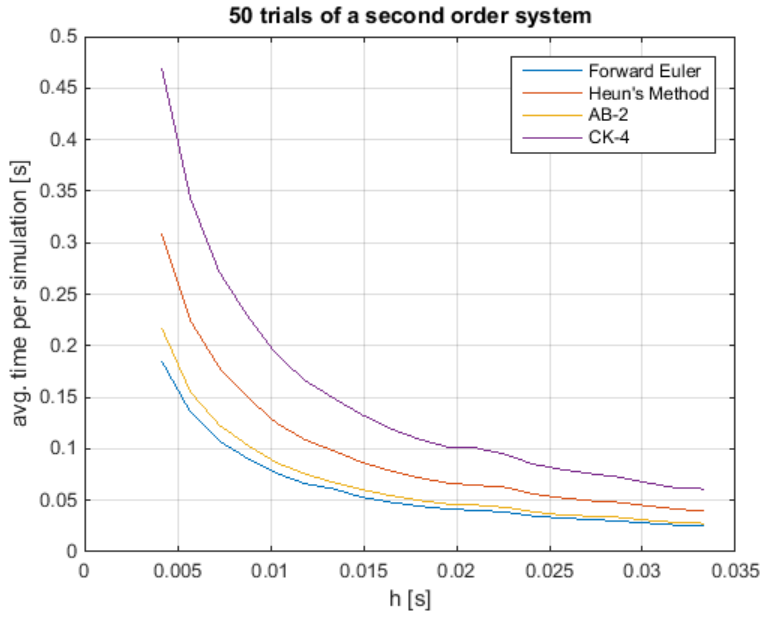

Figure 5.1. Average time per 100s. simulation taken over 50 trials.

We see that average simulation time scales exponentially with step count. On the other hand, as one would expect, average time per iteration is invariant of step size. These results are more interesting in the context of the other factors driving integrator selection. For example, AB-2 is commonly used for power systems simulation software and has good computational performance for the standard quarter cycle step size ($\sim$.004 s). As we will present later, the contender CK-4 has similar, if not more desirable, numerical stability properties as AB-2 at the full cycle step size ($\sim$.016 s). If we extrapolate from the previous experiment, CK-4 is faster than AB-2 when considering the different step size. If the accuracy is comparable or better for CK-4 at this larger step size, it would favor selecting CK-4 for simulation.

5.2 Accuracy considerations

A numerical integration scheme is typically not useful if it is inaccurate. Schemes are typically classified in terms of accuracy by their "order"; this nomenclature is derived from the method's local truncation error, an analytical estimate of how much an integration method differs from the true solution on a step-by-step basis. In this section, we will present two of the metrics we used to examine integrator accuracy and present some experimental results to characterize the four aforementioned integration schemes.

5.2.1 Local truncation error (LTE)

We define local truncation error, τ_n, at each time step n as the difference between the true function value $y(t_n)$ and the function value according to the integration scheme, y_n:

$$\tau_n = y(t_n) - y_n \tag{5.2.1}$$

This quantity is computed assuming that the estimated y_n is calculated based on exact information, i.e., $y_{n-k} = y(t_{n-k})\ \forall\ k > 0$. In other words, it is assumed that all previous iterations of the integration scheme are exactly correct. We can compute τ_n for various integration schemes in order to get a sense of their order of accuracy. For example, we can estimate order of accuracy as related to step size h and even rank different schemes that have the same order of accuracy.

Example 5.2.1 (Forward Euler). To illustrate the process for estimating local truncation error, we will use the Forward Euler scheme as an example. The Forward Euler scheme is defined as:

$$y_{n+1} = y_n + hf_n \tag{5.2.2}$$

where $f_n = y'_n$. Under the correctness assumption for computing local truncation error, this expression becomes:

$$y_{n+1} = y(t_n) + hf_n \tag{5.2.3}$$

Substituting for f_n we obtain:

$$y_{n+1} = y(t_n) + hy'_n \tag{5.2.4}$$

We obtain an equivalent expression for y'_n by performing a Taylor series expansion of y'_n about $(y'(t_n), t_n)$:

$$y'_n = y'(t_n) + hy''(t_n) + \frac{1}{2}h^2 y^{(3)}(t_n) + \mathrm{O}\left(h^3\right) \tag{5.2.5}$$

where $\mathrm{O}()$ indicates higher order terms. Substituting this into the previous expression, we obtain:

$$y_{n+1} = y(t_n) + h[y'(t_n) + hy''(t_n) + \frac{1}{2}h^2 y^{(3)}(t_n) + \mathrm{O}\left(h^3\right)] \tag{5.2.6}$$

Now we need a similar expression for $y(t_{n+1})$. We perform a Taylor series expansion of $y(t_{n+1})$ about $(y(t_n), t_n)$:

$$y(t_{n+1}) = y(t_n) + hy'(t_n) + \frac{1}{2}h^2 y''(t_n) + \mathrm{O}\left(h^3\right) \tag{5.2.7}$$

Now subtract the two expressions to obtain τ_{n+1}:

$$\tau_{n+1} = y(t_{n+1}) - y_{n+1} = -\frac{1}{2}h^2 y''(t_n) + \mathrm{O}\left(h^3\right) \tag{5.2.8}$$

We say this scheme is first-order accurate because the leading term of its local truncation error is proportional to h^2. In general, a scheme is nth-order accurate if the leading term of its local truncation error is proportional to h^{n+1}.

This same process can be done for schemes such as the two-step Adams-Bashforth method and Heun's method, obtaining the following:

AB-2: $\tau_n = \frac{5}{12}h^3 y^{(3)}(t_{n-1}) + \mathrm{O}\left(h^4\right)$
Heun's: $\tau_n = \frac{1}{4}h^3 y''(t_{n-1}) + \mathrm{O}\left(h^4\right)$

In general, according to the orders of accuracy and coefficients of the leading terms, we expect that Heun's $>$ AB-2 $>$ Forward Euler in terms of order of accuracy. We expect that AB-2 and Heun's method perform very similarly for a given system and both to perform better than the Forward Euler method. Additionally, with CK-4 being a fourth order method, we expect it to be the most accurate in terms of local truncation error.

In a stable system, assuming that the system eigenvalues are in the region of absolute stability for all numerical methods, we expect that the solution for all schemes to converge to some final value determined by system parameters. Consequently, we expect the local truncation error for each method to converge to 0 in that scenario and that the order of accuracy correlates with the rate of convergence. We illustrate these observations with some simulated examples.

5.2.2 Example 1: First order ODE

We consider the following inhomogeneous ODE:

$$\frac{\mathrm{d}}{\mathrm{d}t}y(t) = \frac{-y(t) + f(t)}{t_0} \tag{5.2.9}$$

with $y(0) = 0$ where

$$f(t) = u(t) \tag{5.2.10}$$

is the unit step forcing function. This represents a simple first order system with a time constant of t_0. A positive time constant corresponds to negative feedback while a negative time constant corresponds to positive feedback. In the simulation, we "prime" the integration schemes by preceding the forcing function with some number of steps such that the initial conditions hold during that time. It can be verified that the analytic solution to this ODE is:

$$y(t) = (1 - \exp(-t/t_0))u(t) \tag{5.2.11}$$

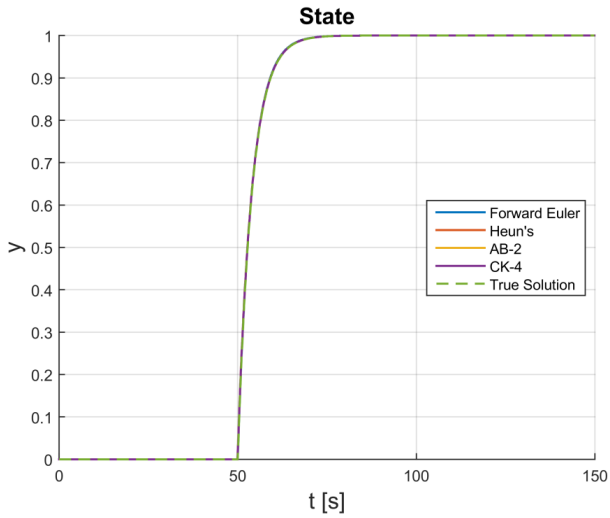

Figure 5.2. Integrated results compared to the true solution. They all pass the eye test of accuracy.

Example 5.2.2 ($t_0 = 4$). This example illustrates a stable system and numerically stable integration schemes. The step size h is chosen to be 0.1.

The result of numerical integration for all schemes appears to match the true solution very well. Looking at the local truncation error as a function of time step shows a different story. Although the two second order and fourth order schemes have a larger local truncation error for earlier time steps compared to the first order scheme, their LTE converge more quickly to 0.

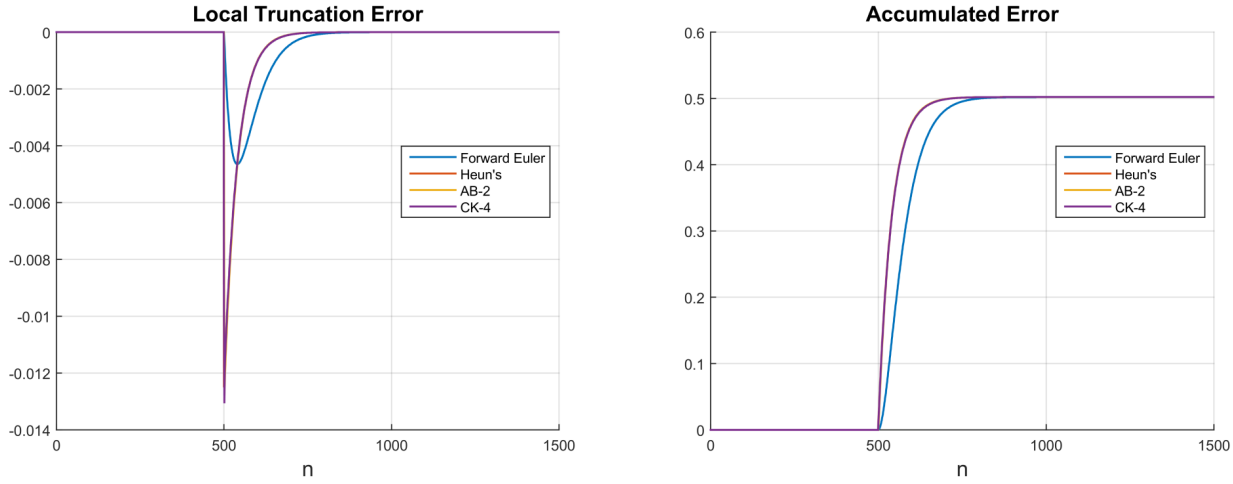

Figure 5.3. Local truncation and accumulated error.

This is also illustrated by looking at the accumulated error at each time step, which we take

to be the absolute sum of the LTE at the current and all previous time steps. Zooming in on the time where the unit step is applied reveals that the higher order methods overshoot the true solution initially, causing the majority of the accumulated error early on. However, we see that they quickly recover and converge to the bound of the cumulative error faster than the first order method does. The bound on each scheme here appears to be identical.

5.2.3 Example 2: Second order ODE

We consider the following 2nd order ODE:

$$\frac{\mathrm{d}^2}{\mathrm{d}t^2}y(t) + b_0\frac{\mathrm{d}}{\mathrm{d}t}y(t) + k_0 y(t) = f(t) \tag{5.2.12}$$

with $y(0) = 0$ and $\frac{\mathrm{d}}{\mathrm{d}t}y(0) = 0$. The characteristic constants are $b_0 = 2\alpha_0$ and $k_0 = \alpha_0^2 + \omega_0^2$ and the system eigenvalue pair is located at $s = -\alpha_0 \pm j\omega_0$. We only consider $\alpha_0 > 0$ and thus are only considering underdamped systems with oscillatory responses. The forcing function $f(t)$ is the unit step function, $u(t)$. It can be verified that the analytic solution to this ODE is:

$$y(t) = \frac{1}{k_0}\left[1 - e^{-\alpha_0 t}\cos(\omega_0 t)\right]u(t) \tag{5.2.13}$$

Example 5.2.3 ($\alpha_0 = 0.5, \omega_0 = 2$). This example illustrates an underdamped system where all three integration schemes are numerically stable. The step size h is chosen to be 0.1. The integration results are more obvious in their differences among the schemes although all schemes do eventually converge to the true solution.

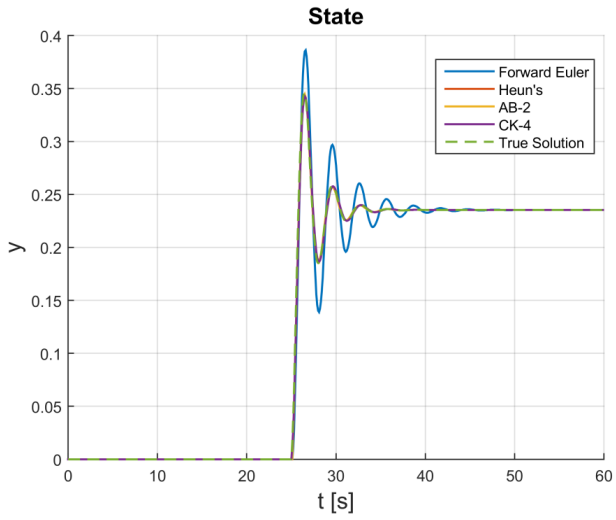

Figure 5.4. Integrated results compared to the true solution. We can start to observe more apparent accuracy differences.

The local truncation error illustrates the major differences. We observe that the first order scheme has a nontrivially larger maximum LTE in addition to converging more slowly to zero LTE as compared to the higher order schemes. In this example, the accumulated error is more indicative of the differences in orders of accuracy among the schemes. Although all schemes have LTE that eventually converge to 0, the accumulated error bound for each is different. The higher order schemes' accumulated errors converge more quickly to similar, lesser values as compared to the first order scheme. However, we notice that the higher order CK-4 method has a marginally larger steady state accumulated error compared to the second order schemes in addition to marginally larger local truncation error at earlier time steps. This does not match the concept of order of accuracy as presented previously. Through experimentation, we found that the CK-4 tends to perform more accurately compared to the second order methods when the eigenvalue pair has a higher frequency.

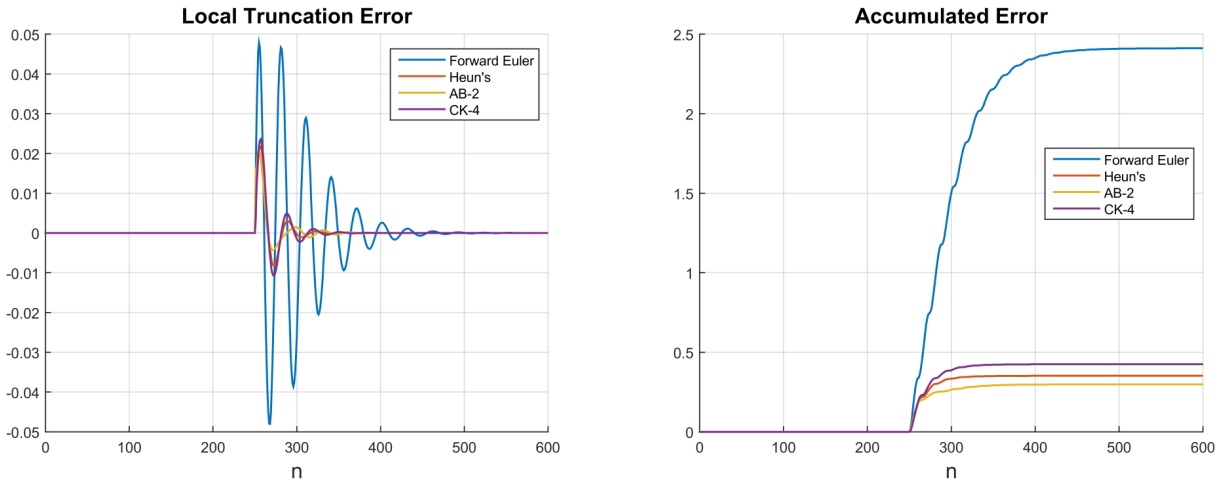

Figure 5.5. Local truncation and accumulated error.

Example 5.2.4 ($\alpha_0 = 0.5, \omega_0 = 5$). In this example, we keep the eigenvalue decay rate the same but increase the frequency. We remove the Forward Euler method results because we've already demonstrated its poor accuracy performance and because it is numerically unstable for the time step and eigenvalue pair location chosen. The results are shown in Figures 5.6 and 5.7.

From the state variable calculations, we can observe how the higher order integration methods start to differ. While CK-4 has no trouble keeping up with the true solution, the two second order schemes start to desync and become out of phase with the true solution within cycles. This manifests into a much slower convergence to zero local truncation error compared to CK-4 and, consequently, a larger steady state accumulated error. In the previous example, we saw an approximate 100% increase in accumulated error between CK-4 and AB-2; here we observe over a sevenfold increase in accumulated error from AB-2 to CK-4.

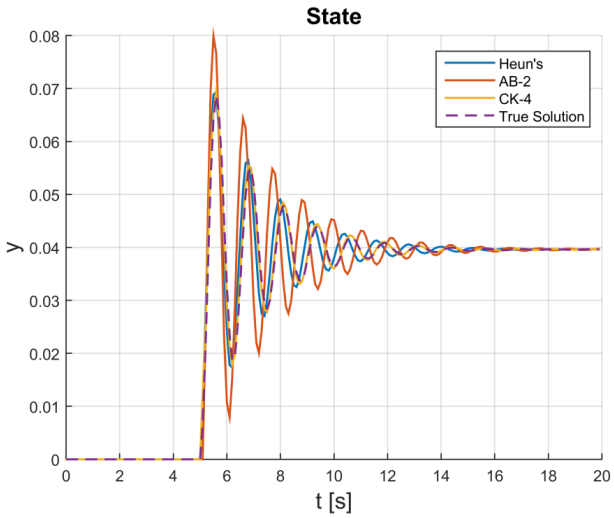

Figure 5.6. Integrated results compared to the true solution. We can start to observe more apparent accuracy differences even among higher order schemes.

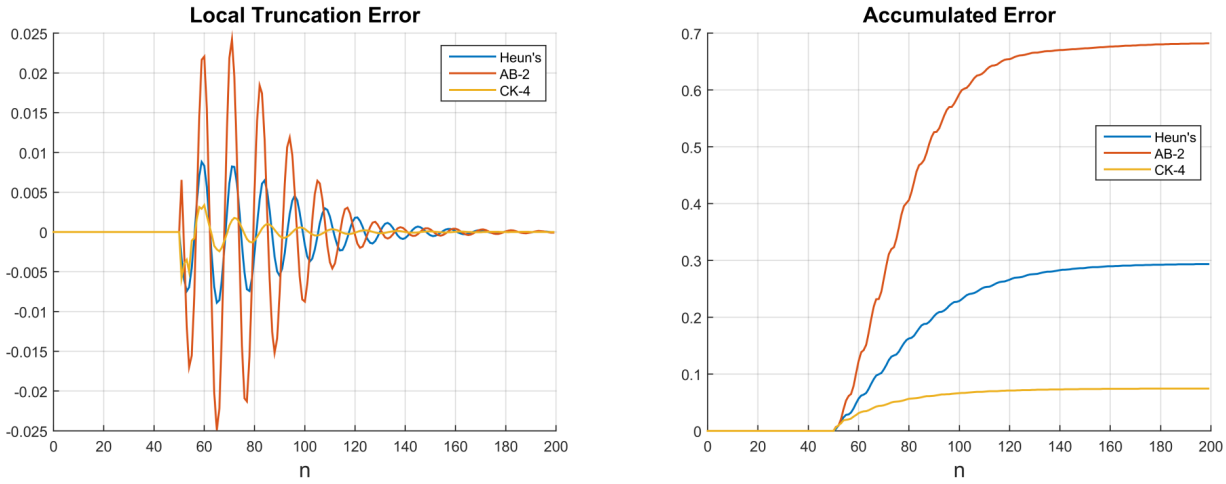

Figure 5.7. Local truncation and accumulated error.

5.2.4 Observations

Analytically, it is unclear why there is such a disparity between these two examples in terms of integrator relative performance. Depending on the dynamical system of interest, it might be worth considering these idiosyncrasies when selecting an integration scheme. However, it is worth noting that the higher order integration schemes seem to perform better in the relative error sense.

The most substantial metric for examining local/global truncation error is far and away the order of accuracy. Among integration schemes with the same order of accuracy, the differences in LTE/accumulated error and convergence to the true solution are minute, regardless of the coefficient on the leading term of the LTE. Admittedly, this is based on a very small sample size of integration schemes. The differences among integration schemes with different orders of accuracy, however, are significant.

The seemingly obvious choice is to choose the highest order of accuracy integration scheme for the best integration performance. However, as we observed, the computational burden for higher order schemes increases at a superlinear rate as method order increases. In the next section, we will examine the final facet of numerical stability and summarily illustrate the tradeoffs when selecting an integration scheme.

5.3 Numerical stability considerations

Previously, we touched on the general concepts of relative and absolute stability in the context of numerical integration methods. In particular, we looked at the relationship between system dynamic stability and integrator numerical stability in terms of system eigenvalue locations. In this section, we will revisit these concepts, specifically for the four integration methods under investigation.

5.3.1 Region of absolute stability

The procedure for calculating the region of absolute stability was outlined as follows:

1. State the recurrence relation determined by the numerical method.
2. Compute and solve the characteristic polynomial for its roots.
3. The region of absolute stability is the region in which all roots of the characteristic polynomial have a magnitude strictly less than unity.

This region is defined in the $\bar{h} = h\lambda$ complex plane, where h is the step size in seconds and λ is the complex eigenvalue. Hence, the region needs to be scaled by the step size in order to compare it to system eigenvalues. For lower order multistep methods, deriving the region of absolute stability analytically is tractable. For higher order methods (> 2), computing the region needs to be done numerically. Figure 5.8 shows the regions of absolute stability for the four integration methods of interest in the $h\lambda$-plane.

All methods include some subset of the left plane, which encompasses all eigenvalues for dynamically stable systems. Here we can observe the characteristic shape of CK-4: thin near the

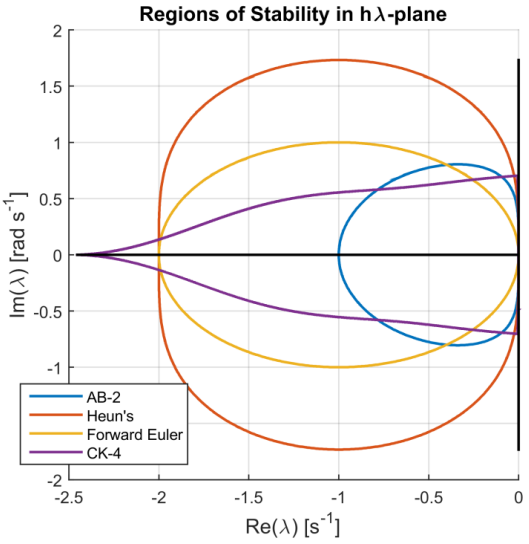

Figure 5.8. Region of absolute stability for the integration methods in the $h\lambda$-plane.

$j\omega$-axis like AB-2, but extends out far along the real axis like Heun's method but even further into a characteristic cusp.

In Figure 5.9, we scaled the regions of absolute stability to the s-plane for two step sizes of interest — quarter cycle and full cycle. As we observed in the stiffness analysis for the two cases, the limiting eigenvalues for system stiffness tended to be those related to the dynamics of the exciters; in particular, they were related to the time constants of the voltage transducers in the exciter models. For time constants on the order of 10 to 20 ms, the corresponding system eigenvalues were located at -50 to -100 on the real axis. For a time step of a quarter cycle, these eigenvalues fit comfortably in the region of absolute stability for all integrators, including the oft-used AB-2. However, for a full cycle time step, AB-2 begins to run into trouble numerically due to its relatively truncated region of absolute stability. Due to the characteristic cusp of CK-4, one can imagine that if the limiting eigenvalues are known ahead of time, if CK-4 is used to integrate, then the time step can be selected precisely such that the limiting eigenvalues fit within the region of absolute stability.

5.3.2 Numerical oscillations

Previously, we demonstrated what effect absolute stability has on numerical integration. Although absolute stability guarantees the simulated solution will eventually converge to the true solution, this does not exclude less than desirable phenomena such as numerical oscillation from occurring. Empirically, numerical oscillation directly correlates with proximity to the region of absolute stability boundary. As system eigenvalues encroach on the boundary from within the region, nu-

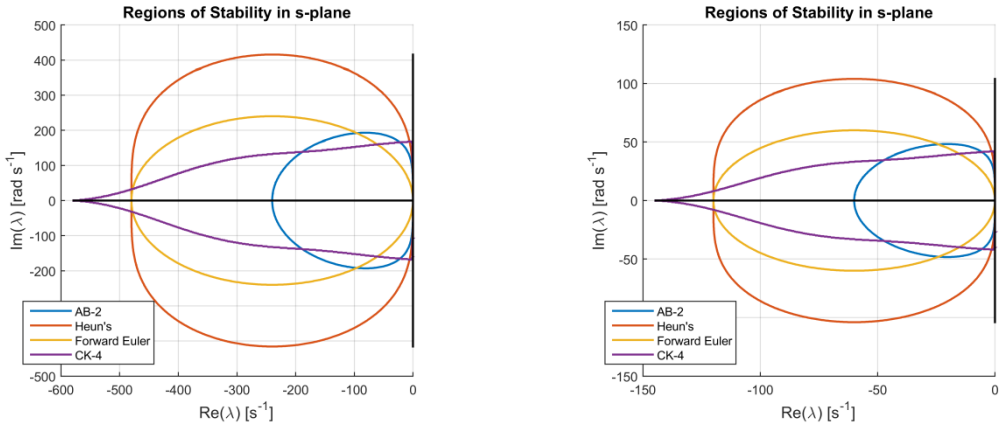

Figure 5.9. Regions of absolute stability for two different step sizes. (left: quarter cycle, right: full cycle)

merical oscillation severity seems to increase. Using the previous example, we can demonstrate this phenomenon. The step size of choice and the system eigenvalue locations create a situation in which the system eigenvalues are very near the boundary of the region of absolute stability for AB-2.

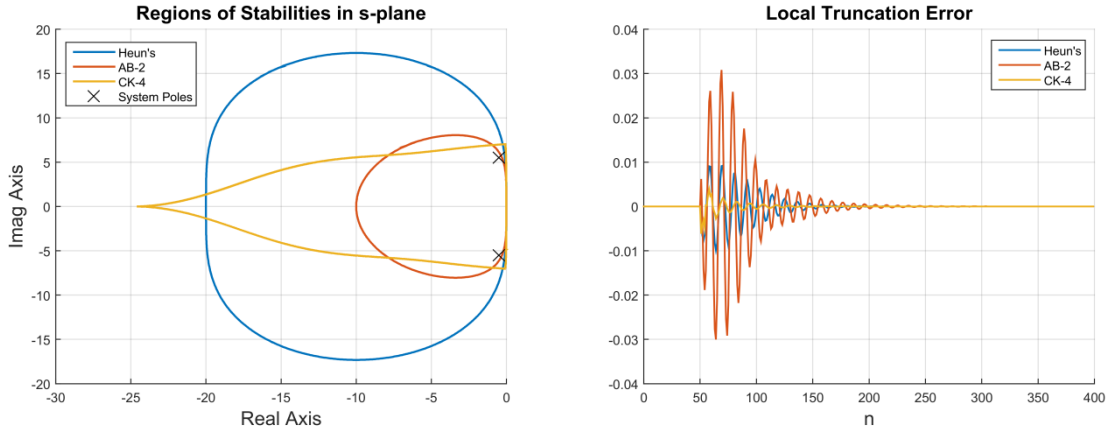

Figure 5.10. System eigenvalue map and LTE for corresponding simulation.

Refer to the previous section to see the calculated system state. While the solution using AB-2 eventually does converge to zero local error and the true final value, the state variable time series as simulated is fundamentally different from the true solution. The decay rate is significantly slower compared to the more accurate simulated solutions and it is significantly out of phase with the true solution. Furthermore, there is significant overshoot and undershoot as simulated as well as a slight frequency depression. These issues can potentially cause false alarms if, for example,

there are controls that respond to voltage limits or frequency dips. So while absolute stability should be the primary factor when considering the numerical stability of potential integrators, the actual "effective" region of absolute stability is most likely smaller than depicted due to numerical oscillation concerns.

5.3.3 Numerical stability demonstrations with PST

By modifying the PST code, we implemented AB-2 and CK-4 as integrator choices in PST. While simple second order systems possess the transparency that makes it easy to compare aspects of numerical integration such as accuracy, this analysis was ultimately for selecting an integration scheme for power system simulation. In the next few examples, we will demonstrate how numerical stability affects dynamic simulation.

Example 5.3.1 (Instability of AB-2). We used the KRK system with half of the exciters having voltage transducer time constants of 10 ms, resulting in eigenvalues at approximately -100 s^{-1}. We fixed the integrator time step at a full cycle; it can be verified that this causes the exciter system eigenvalues to lie outside of AB-2's region of absolute stability but inside those of Heun's method and CK-4 (c.f. Figure 5.9). To excite system modes, we simulated a three-phase fault like what was done in the time domain analysis.

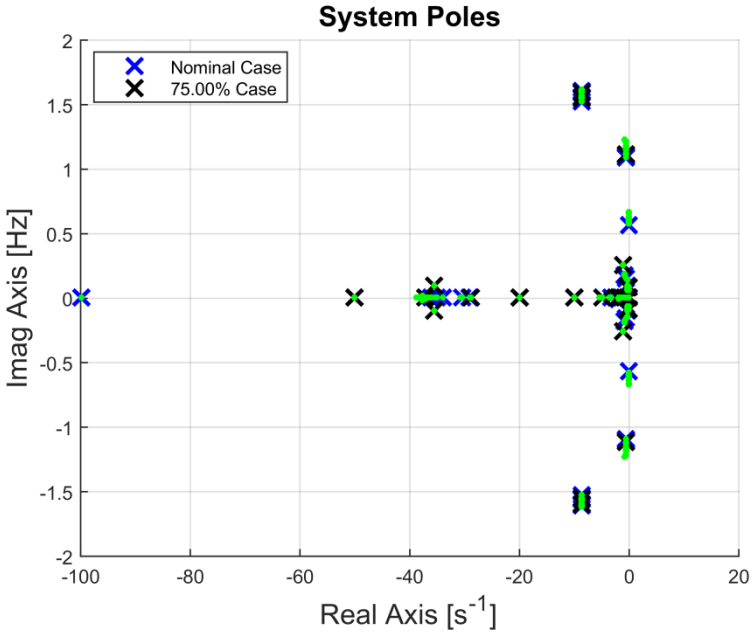

Figure 5.11. System eigenvalue map for transient response simulation.

Figure 5.12 shows the simulated responses using Heun's method and CK-4. Qualitatively, they appear similar to the response that one would expect. Figure 5.13 shows the simulated response

using AB-2. The simulation actually froze and failed to complete the entire simulation duration (30 seconds). We can observe that the simulated solution is already showing divergent behavior before the software hung.

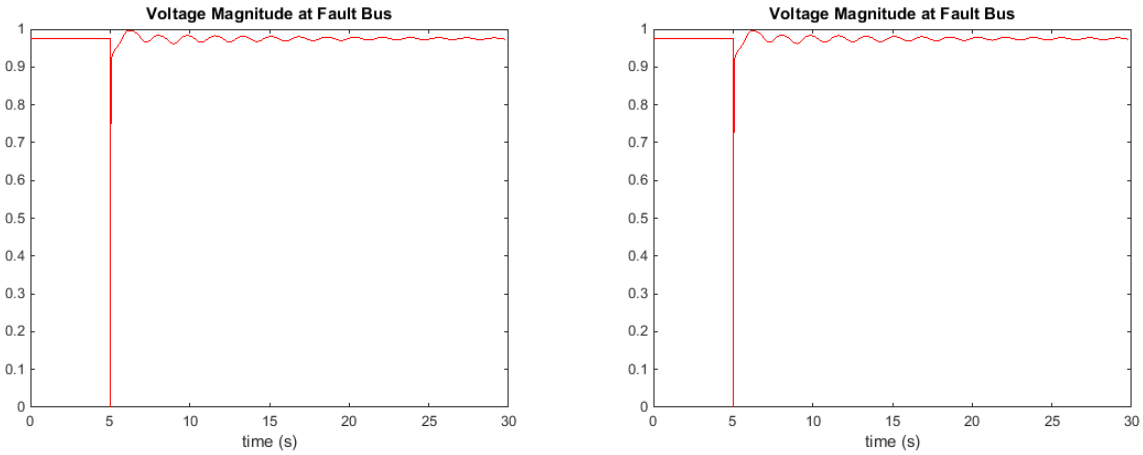

Figure 5.12. Transient response as simulated using Heun's method and CK-4.

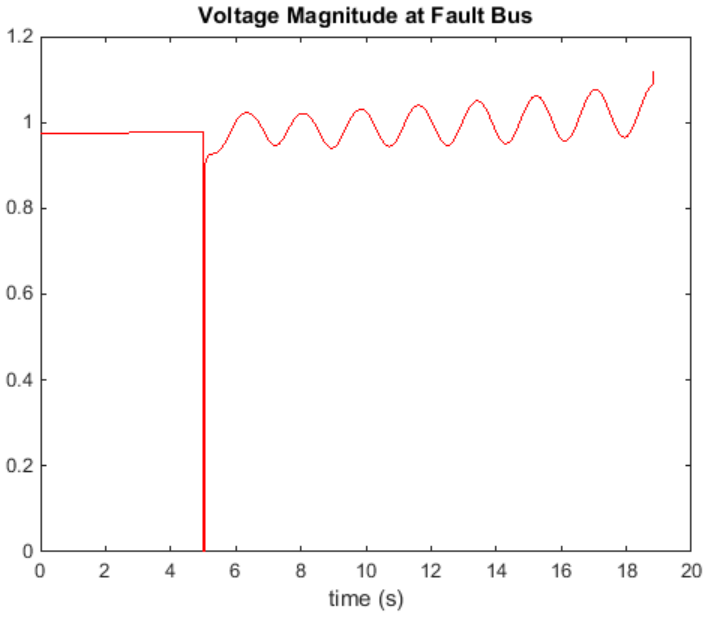

Figure 5.13. Transient response as simulated using AB-2.

Example 5.3.2 (CK-4 stability). In another demonstration, we adjusted the step size and exciter time constants such that one eigenvalue is inside the region of absolute stability for CK-4 but outside those of the other integrators. The simulation results are in Figures 5.14 and 5.15. As one would expect, we observe divergent behavior for the integrators for whom the simulation is numerically unstable. On the other hand, while the simulation using CK-4 is numerically stable, we can observe some numerical oscillation following the fault clearing shortly after 5 seconds. As alluded to previously, since there are system eigenvalues located near the cusp at the far end of the real axis, we expect some amount of numerical oscillation. However, in the end, only the simulation that used CK-4 was able to complete the simulation with any semblance of fidelity.

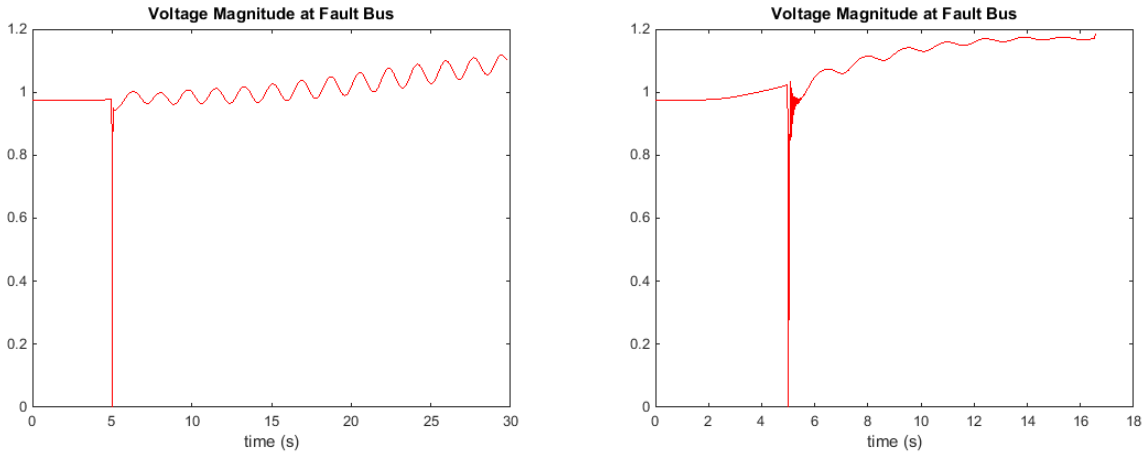

Figure 5.14. Simulation results using integrators that are numerically unstable. (left: Heun's method, right: AB-2)

5.3.4 Power system eigenvalue topology and selecting an integrator

With numerical stability as the priority criterion for selecting an integrator, it is vital to understand the general eigenvalue topology for the typical power system to be simulated. In general, power system models typically contain the same component dynamic models with associated system eigenvalues in the same region of the complex plane; there is variation in eigenvalue location due to actual parameter values. To illustrate this point, we used a 16 machine test case containing 29 induction motor loads. In Section 4, we presented a system eigenvalue topology map derived from this test system, shown again in Figure 5.16.

Using the methodology for mode identification and state association used in Section 4, we annotated the eigenvalue map to indicate what dynamic models are associated with various regions in the complex eigenvalue plane. While the two example systems we analyzed in depth did not contain them, induction motor load models are most likely to restrict the selection of an integrator due to their fast decaying, high frequency modes. Most commonly, the time constants associated with transient and subtransient machine models, exciters, and PSS will stress the selection of an

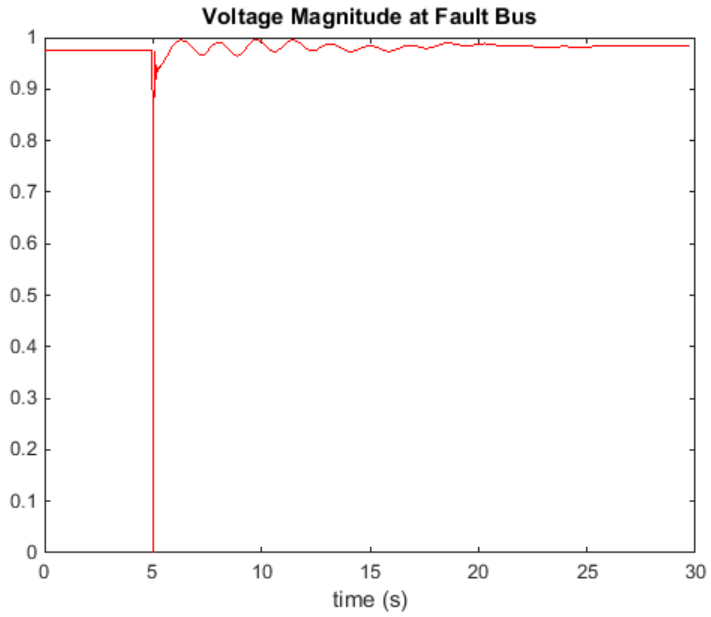

Figure 5.15. Simulation results using CK-4 which is numerically stable. Note the brief numerical oscillations following the fault clearing.

integrator and/or step size. The region annotated on the eigenvalue map is directly correlated to these time constants, which are typically in the 20 ms or smaller range. The dynamics associated with these time constants are far and away the fastest dynamics in power system models that do not contain induction motor loads. Due to region of absolute stability shapes for typical explicit integration schemes, these time constants will most likely restrict how large the step size can be. The other two regions identified are highly unlikely to affect the choice of integrator and step size; these relatively slower decaying, low frequency modes will almost surely be well within the region of absolute stability for any integrator unless all of the aforementioned time constants happen to be very large. Additionally, the `pwrmod` model used to model PV current injections has associated eigenvalues at -20 s^{-1} due to 50 ms time constants. As noted previously, increased PV penetration, as modeled, has no definite effect on system stiffness. Integrator selection stress does not directly come from the presence of PV-related current injections, but rather from the tendency for system eigenvalues to drift left with increased PV penetration.

5.4 Conclusions

One of the reasons for considering different integrators for extended-term simulation of power systems with high PV penetration is that for very long simulation lengths, it is less feasible to use integrators with the oft-used quarter-cycle timestep due to computation speed and data storage

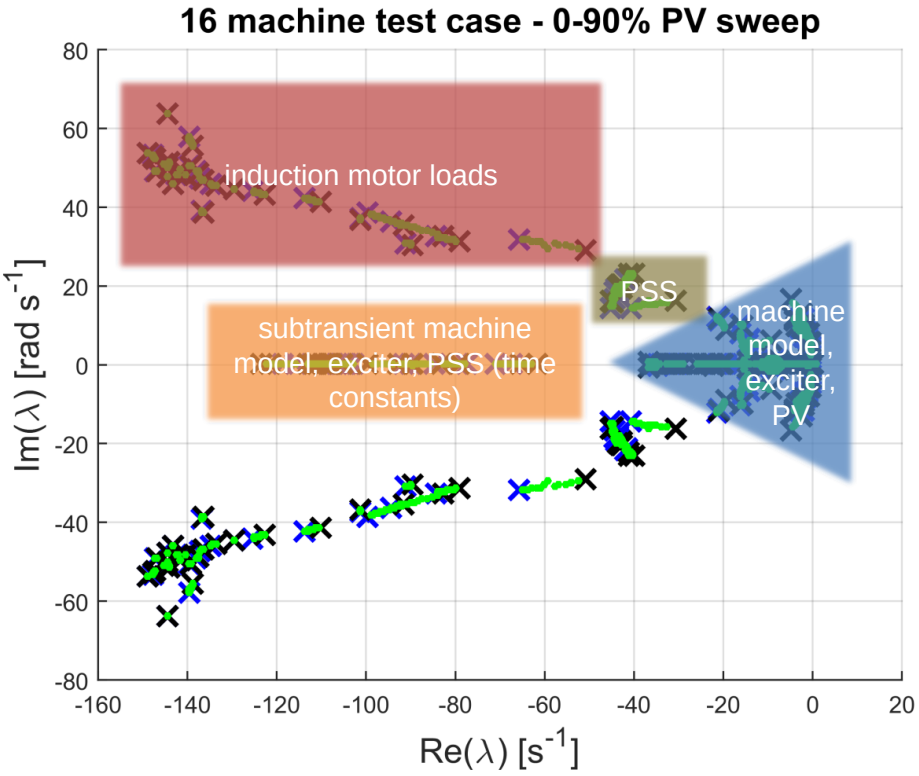

Figure 5.16. System eigenvalue map for 68 bus system with typical eigenvalue locations for common power system model components.

bloat. Based on our analysis, the ubiquitous AB-2 with a quarter-cycle timestep is very capable for most power systems to be simulated and is perfectly suitable for shorter duration simulations. For simulations of durations exceeding the minute mark, increasing the timestep to, i.e., a full cycle would be a massive improvement in terms of computation time and data storage management. Because of its unique numerical stability properties, we recommend CK-4 as an integrator because it tends to be highly compatible with many power system models; additionally, it gives the most real estate in terms of absolute stability where it matters for a given step size. As a result, one is most likely able to reduce the simulation step size using CK-4 than the other integrators. While this comes at the cost of additional computation time, based on our analysis, it might actually be faster to use CK-4 than other integrators because other integrators are more likely to require a smaller step size for numerical stability.

One drawback of using CK-4 is its thinner region of absolute stability in the frequency sense. From the example of the system with induction motor loads, this property tends to be problematic for CK-4 because of the existence of large decay rate, high frequency modes. The presence of these

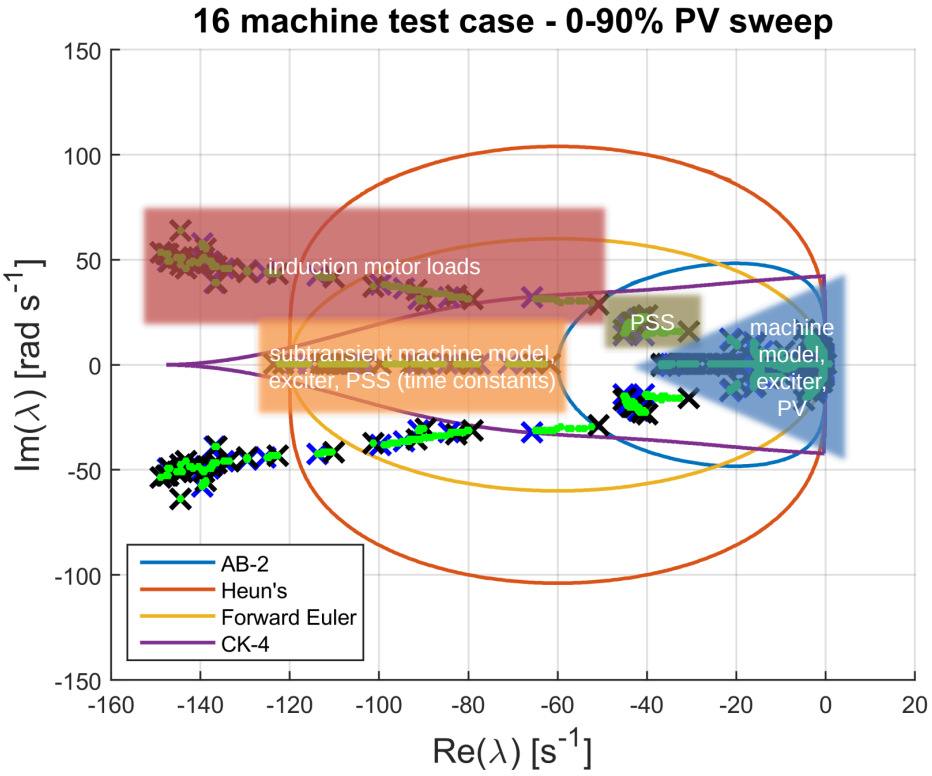

Figure 5.17. System eigenvalue topology with region of absolute stabilities $h = \frac{1}{60}$ s overlaid.

modes requires CK-4 to use a larger step size to be numerically stable when simulating this type of system and eliminates the advantage of CK-4. For this reason, we recommend using Heun's method as it contains much more bandwidth for a given step size. Figure 5.17 illustrates how the regions of stability at a full cycle time step compare to the archetypical system eigenvalue map.

In general, we recommend using small signal stability studies or having some knowledge of the dynamics of a power system to be simulated in order to make an intelligent selection of a numerical integration method. For general purpose, versatility, and safety, we recommend Heun's method because of its relatively large region of absolute stability, ease of implementation, and reasonable computational performance. For extended-term simulations, we recommend CK-4 whenever the characteristics of the power system model allow for it because of its potential to increase the fixed simulation step size and reduce the number of iterations and data storage required.

In the next two sections, we discuss two alternatives to fixed time step, explicit integration schemes for extended-term dynamic simulations with very high PV penetration levels. The next section on variable step size integration introduces the class of numerical methods that allow the simulation to intelligently adapt the time step to the types of dynamics present. The proceeding

section on slow system dynamics offers a shift in the framework and paradigm of how power systems are modeled and simulated based on an identified gap of simulation capabilities.

This page intentionally left blank.

Chapter 6

Variable step size integration

In transient stability analyses, a power system is represented by a set of ordinary differential equations (ODEs) and a set of algebraic equations. As a consequence of this formulation, the overall power system representation consists of a set of differential-algebraic equations (DAEs) of the following form:

$$\text{(differential)} \qquad f(x,v) = x' \tag{6.0.1}$$

$$\text{(algebraic)} \qquad g(x,v) = Yv - i(x,v) = 0 \tag{6.0.2}$$

where:

$x = m \times 1$ vector of state variables
$v = n \times 1$ vector of complex bus voltages (real and imaginary parts)
$i = n \times 1$ vector of current injections at each bus (real and imaginary parts)
$Y = n \times n$ network admittance matrix

A conceptual representation of (6.0.1) and (6.0.2) is shown in Figure 6.1. The figure shows the dual nature (differential and algebraic) of the power system representation used in transient stability studies.

In general, a numerical algorithm for solving (6.0.1) and (6.0.2) computes the values of state variables and bus voltages at discrete times, e.g., $t_1, t_2, ..., t_{n-1}, t_n$. In the vast majority of transient stability analyses, these times are equally spaced. The time between consecutive time steps is the time step of integration and is typically denoted by Δt or h. Typical time domain simulations for power system planning studies cover a time frame spanning 15-30 seconds and the simulations are performed using a constant time step of integration with a value in the order of 1/4 of a cycle (0.004167 sec in a 60 Hz system).

The recent widespread introduction of photovoltaic and wind power plants suggest the need to consider extending simulation time frames beyond those associated with transient stability studies to take into account the variable nature of solar and wind power over extended time periods. One possible approach for addressing the issue of extended simulation times, while also allowing for the

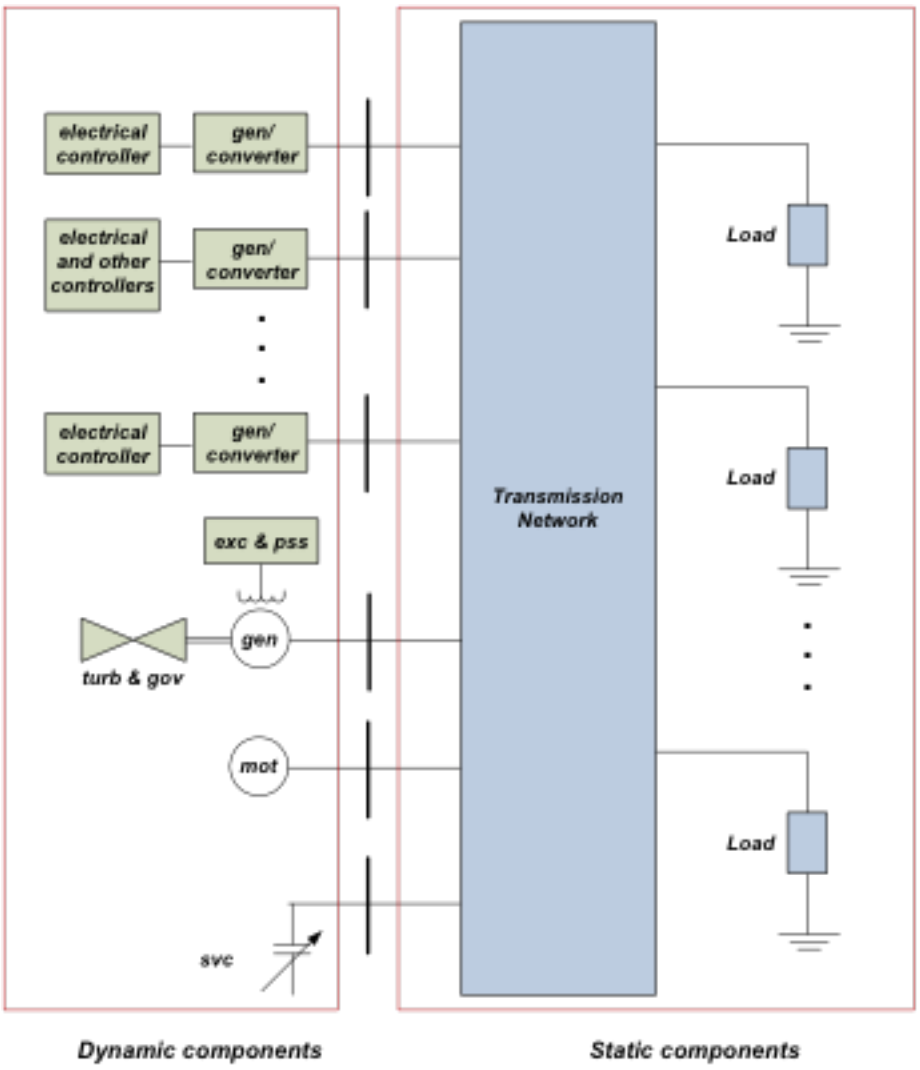

Figure 6.1. Power system topology.

representation of system dynamic phenomena associated with traditional transient stability studies, is to use a variable time step of integration. In this approach, the time step of integration is allowed to increase as fast transients subside; conversely, the time step of integration is reduced to capture faster transients.

The objective of this section is to provide a high level overview of various considerations involved in the development of a variable time step simulation algorithm for solving (6.0.1) and (6.0.2). Recognizing the existence of multiple algorithms for adjusting the time step of integration, subsequent paragraphs describe considerations and procedures that have been found to be practical and effective.

6.1 General considerations

Although a large number of numerical methods are available for solving sets of ODEs, the inherent characteristics large power systems impose severe constraints on the type of numerical algorithms that can be used effectively to study power system dynamics. Size, diversity of components, and sudden switching events are among the power system characteristics that restrict the application of many numerical methods to the study power system dynamics.

An effective algorithm does not impose an excessive computational burden, provides the required accuracy, includes an efficient adjustment of the time step of integration, and also allows for the use of relatively large time steps of integration when the system is in quasi-steady state.

Depending on the solution algorithm for the ODEs and on whether (6.0.1) and (6.0.2) are treated as a single set or two separate sets of equations, the solution algorithms can be classified as:

- Partitioned-Explicit (PE)
- Simultaneous-Implicit (SI)
- Partitioned-Implicit (PI)
- Simultaneous-Explicit (SE)

The terms Explicit and Implicit refer to the method of solution associated with the differential equations; the terms Partitioned and Simultaneous indicate whether the equations are solved as a single set of equations or two separate sets. Thus, in the PE approach (6.0.1) and (6.0.2) are treated as two separate sets of equations and the differential equations are solved using an explicit method, e.g., Adams-Bashforth, Explicit Runge-Kutta. In the SI approach, (6.0.1) and (6.0.2) are treated as a single set of equations and the differential equations are solved using an implicit method, e.g., Adams-Moulton, Gear's method.

The PE and SI approaches are the solution methods that, by and large, have been implemented in commercial software packages for bulk power system analysis, e.g., PSLF, PSS/E, PowerWorld, Eurostag, DigSilent. For solution algorithms that use a variable time step of integration, the SI approach is preferred. This is the approach referred to in subsequent paragraphs.

6.2 Analytical formulation

Here, a simple second order integrator, the trapezoidal method, is used for illustration purposes. The trapezoidal method is a member of the Adams-Moulton family and it is suitable for power system dynamic simulations. The trapezoidal method is given by:

$$x_{k+1} = x_k + \frac{1}{2} h_k [\dot{x}_{k+1} + \dot{x}_k] \tag{6.2.1}$$

In (6.2.1), h_k is the time step of integration at time k. Solving for the derivatives at time $k+1$ in (6.2.1):

$$\dot{x}_{k+1} = \frac{2}{h_k} [x_{k+1} - x_k - \frac{1}{2} h_k \dot{x}_k] \tag{6.2.2}$$

The solution of (6.0.1) and (6.0.2) is accomplished by replacing the derivatives in (6.0.1) by their discrete approximation given in (6.2.2):

$$\frac{2}{h_k} [x_{k+1} - x_k - \frac{1}{2} h_k \dot{x}_k] - f(x_{k+1}, v_{k+1}) = 0 \tag{6.2.3}$$

$$i(x_{k+1}, v_{k+1}) - Y v_{k+1} = 0 \tag{6.2.4}$$

(6.2.3) and (6.2.4) constitute a single set of algebraic equations of the form:

$$F(x_{k+1}, v_{k+1}) = 0 \tag{6.2.5}$$

(6.2.5) is solved at each time step using a suitable nonlinear solver such as the modified Newton method where at the ith iteration the unknowns are updated as follows (α is a deceleration factor < 1) :

$$x_{k+1}^{(i)} = x_{k+1}^{(i-1)} - \alpha \Delta x \tag{6.2.6}$$

$$v_{k+1}^{(i)} = v_{k+1}^{(i-1)} - \alpha \Delta v \tag{6.2.7}$$

Δx and Δv are the solution of the set of linear equations:

$$J \begin{bmatrix} \Delta x \\ \Delta v \end{bmatrix} = \begin{bmatrix} r_x \\ r_v \end{bmatrix} \tag{6.2.8}$$

where:

$\Delta x = m \times 1$ vector of state variable corrections
$\Delta v = n \times 1$ vector of bus voltage corrections (real and imaginary parts)
$J = (m+n) \times (m+n)$ Jacobian matrix
$r_x = n \times n$ differential equation residual from Equation 5
$r_v = n \times 1$ algebraic equation residual from Equation 6
$\alpha = n \times 1$ deceleration factor

The Jacobian matrix, J, is of the form:

$$J = \begin{bmatrix} J_{11} & J_{12} \\ J_{21} & J_{22} \end{bmatrix} \tag{6.2.9}$$

$$J_{11} = \frac{2}{h_k} I - \frac{\partial f}{\partial x} \tag{6.2.10}$$

$$J_{12} = -\frac{\partial f}{\partial v} \tag{6.2.11}$$

$$J_{21} = -\frac{\partial i}{\partial x} \tag{6.2.12}$$

$$J_{22} = Y - \frac{\partial i}{\partial v} \tag{6.2.13}$$

The initial values for the Newton solver are computed with an explicit integrator and are the so-called predicted values. The Newton solver computes the "corrected" values. This type of solution algorithm is known as a predictor-corrector method.

6.3 Time step control

When time step adjustment is part of the solution algorithm, the time step needs to be adjusted such that the required accuracy for a given simulation case is achieved. Conceptually, if the solution is smooth, then relatively large time steps should be feasible; conversely, if the solution is varying rapidly, then the time steps should be small enough in order to capture the changes in the system variables.

The time step is increased only if two conditions hold: a) the local error is small enough (below a given tolerance) for a pre-specified number of time steps and b) the time step can be increased by a substantial amount, e.g., by a factor of two, based on the local error. The first condition leads to good performance and the second avoids refactoring the Jacobian matrix too often.

The time step is reduced if the local error exceeds a given tolerance or if the Newton solver requires an excessive number of iterations. Also, if a switching event or fault occurs, rather than using a mathematical formula, reducing the time step to the value used in transient stability simulations provides an efficient approach. An additional feature that has been found to be effective in the presence of switching events and faults is to use an explicit low order integrator rather than an explicit integrator. The former does not require the use of a Newton solver to solve the combined set of differential and algebraic equations (i.e., (6.2.5)), provides the required accuracy, and is numerically stable with small time steps. Once the transients subside, the algorithm can revert to an implicit formulation.

A flow chart showing the main functions of a variable time step formulation using an implicit integrator is shown in Figure 6.2.

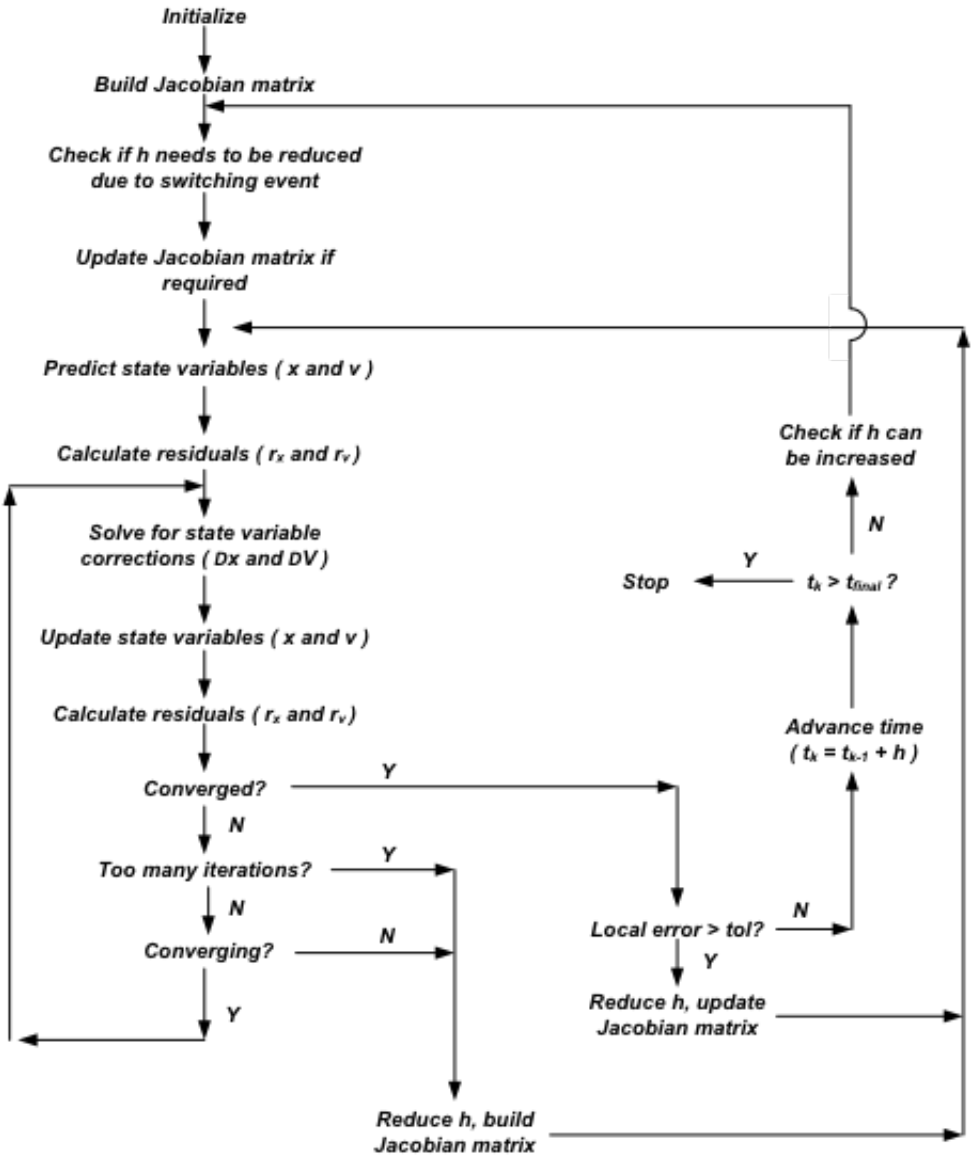

Figure 6.2. Simulation algorithm flowchart.

Chapter 7

Slow system dynamics modeling

Some of the first coordinated technical efforts related to PV integration contemplated primarily small-scale distributed generation which was expected to be connected at distribution voltages. One of the outcomes of these early efforts was the IEEE 1547 standard, which concerned itself primarily with three areas: safely disconnecting the PV resource from de-energized feeders (the frequency drift test), preventing the PV resource from actively controlling feeder voltage, and minimizing interference due to harmonics [12]. As the industry's technical understanding matured, more effort was devoted to the impacts of large-scale PV integration. Specifically, subject matter experts began to explore the impacts of large-scale PV deployment on power system stability. As stated in SNL's PV interconnection requirements report, "The power system is dynamic system and, as such, the full spectrum of possible behaviors cannot be predicted with a steady-state, static model. Dynamic issues within the power system, such as transient stability of rotating machines (generators and motors), are addressed using transient stability programs that examine the system from tens of milliseconds up to several seconds after an event" [8]. By 2010 the industry was standardizing study methods for static analysis of large-scale PV [20], and by 2014 study methods and models for transient stability studies were also being standardized[9].

Tools and methods to study high PV penetration scenarios are presented in Table 7.1. By extending previous analyses to consider 100% PV penetration scenarios, the outcomes embodied in this report might be viewed as a milestone demonstrating that the technical community now has a full understanding of the tools and methods required to conduct planning studies contemplating any level of PV penetration. The approach follows that of the basic modeling/simulation framework for power system studies that has evolved over several decades in accordance with the needs of power system planners and operations staff. The existing framework involves modeling and simulation in three distinct timeframes: steady-state models and studies to investigate system loading conditions and voltage profiles; "transient stability" models and simulation tools to investigate primarily the electro-mechanical interactions of classic rotating generators with one another; and "electro-magnetic transient" models and simulation tools to investigate high-speed phenomena such as lightning strikes. For each of these three timeframes, power engineers have devised models and mathematical solution techniques appropriate to the problem.

This focus of this study is to Identify the characteristics and requirements for large-scale simulation of a power grid with PV generation equal to 100% of load. This study, and other large-scale integration studies that have preceded it, devote considerable attention to transient and small-signal stability impacts of high PV scenarios. The authors note, also, that the industry is experienc-

Table 7.1. Types of system studies.

Type of study	Timescale	Toolset	Examples of Phenomena of Interest Within the TImescale
Electro-Magnetic Transients (EMTP)	10^{-6} to 10^{-2} seconds	Full three phase simulation with all components modeled as differential equations. Equivalent to SPICE simulation.	• Faults • Voltage spikes • Harmonics
Transient Stability	10^{-2} to 100 seconds	Usually positive sequence simulation with reactive network components modeled as algebraic equations. Controller models can use differential equations.	• Inertia dynamics • Generator controls • Induction motor stalls
(capability gap)	100 seconds to hours	No standard toolset exists. Sometimes these studies are conducted by examining a set of power flow cases. Operator training simulators have these capabilities, but the models are simplistic.	• Automatic Generation Control • FIDVR • Frequency response
Steady state (static)	Hours to years	Positive sequence power flow involves solving a set of nonlinear algebraic equations. This is not a time-step simulation.	• Equipment overloading • Low voltage conditions (static) • Reactive resource management • System losses and economics

ing substantive and challenging issues related to maintaining the supply/demand energy balance during rapid PV ramps as well as reactive resource management issues associated with high PV penetration scenarios.

7.1 Issues associated with current simulation framework

Transient stability tools and methods are not well suited to study certain issues related to high PV penetration scenarios such as ramps, reactive resource management and long-term phenomena. PV sources are inverter-coupled, and so they do not exhibit the electro-mechanical properties of classic rotating generators. Furthermore, PV sources are generally intermittent and therefore they pose new and previously under-studied issues to the power engineering community. For example, the timeframes associated with PV intermittency is very difficult to model with classical transient stability simulation tools. Those tools are not well equipped to incorporate AGC action or dynamic

redispatch algorithms, and the component models representing, for example, AGC controllers are not universally accepted.

Consider, for example, a hypothetical PV generating station having a contractual obligation to deliver capacitive VARs to support voltage at a transmission bus serving as the point of interconnection. The contract terms might require the PV owner to provide voltage support during operating conditions in which POI bus voltage is below nominal for a specified duration. This represents a relatively simple requirement; however there are no universally accepted study tools and/or methods that allow the technical community to study system-wide impacts of this sort of requirement.

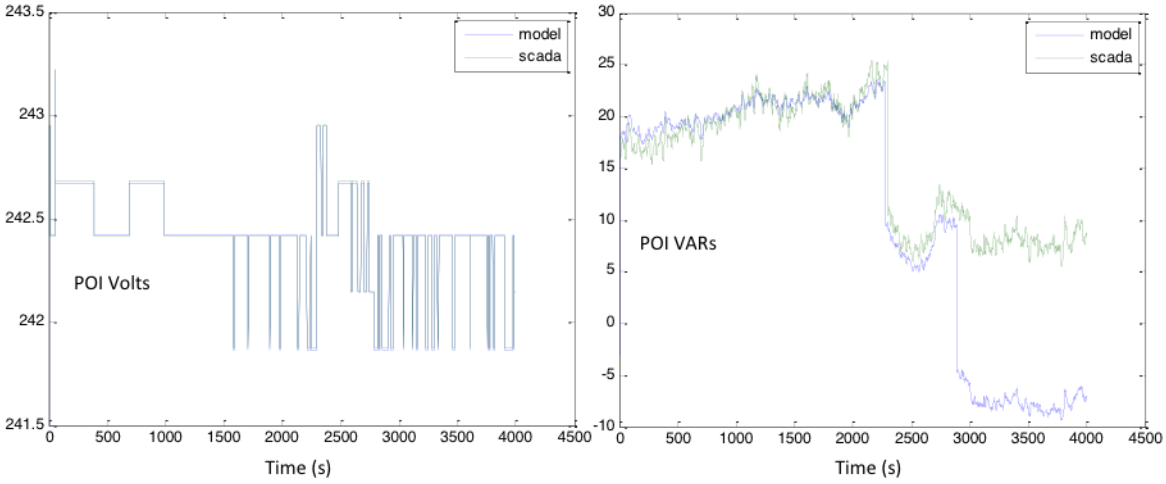

Figure 7.1. Comparison of actual versus predicted reactive support.

Figure 7.1 illustrates such a case. On the left is POI bus voltage, both measured and simulated. Measured and simulated values are generally equivalent throughout the study. Parenthetically, the quantization effect is due to limitations of the SCADA measurement system. On the right is MVARs delivered from the generating station. Note that the model predicts the generating station will deliver additional VARs at approximately t = 2800 s, when POI bus voltage began to show a downward trend. However the measured data does not demonstrate the predicted behavior. The study was carried out by solving thousands of sequential power flow cases while invoking timers on specific process variables within the simulation. Simulating this case with transient stability software was deemed to be inappropriate due to the duration of the simulation. While this toolset and study methodology was found to be useful in this case, the tools and methods are inflexible and not well suited for more detailed analysis.

Management of reactive resources is not the only issue motivating the need for new tools and methods to study long term dynamics. Real power management has also proven to be a significant issue related to integrating utility-scale PV, and an issue that must be well understood as PV penetration increases toward 100%. Figure 7.2 depicts a generic model for Automatic Gen-

eration Control (AGC) as described by Prowse [21]. The purpose of AGC is to compensate for overall energy imbalance by managing dispatchable generation, called "Controlled Generation" in the reference. AGC and other automatic schemes for dispatching controllable generation and load resources play an important role during PV ramps. The model incorporates very slow dynamics, i.e. very long time constants, for filtering and integrating.

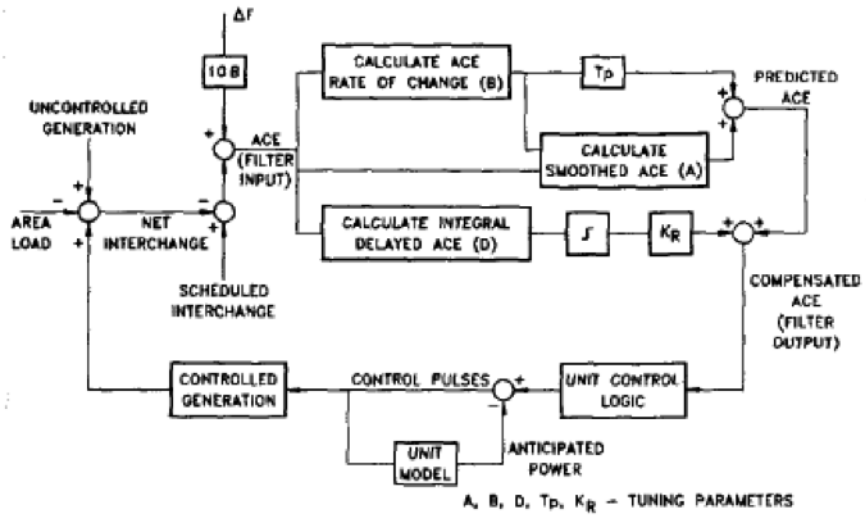

Figure 7.2. An AGC algorithm from [21].

There is a need to modify our existing suite of power system simulation tools to incorporate longer term control action such as AGC or dispatching on 5-minute schedules. Two approaches are examined herein: variable time step simulations and adaptive modeling. The two approaches are complimentary, i.e. it is prudent and appropriate to increase the simulation time step within a transient stability simulation when "fast" dynamics have settled. It is equally appropriate to "swap out" portions of component models that are no longer necessary to study the phenomenon of interest. Variable time step simulation was examined in Section 6.

7.2 Adapative modeling approach

In transient stability simulations it is customary to model the inertia dynamics of large rotating electro-mechanical conversion devices such as synchronous generators along with controllers, e.g. exciter and governor, designed to manage voltage and power characteristics of the generator as it relates to the grid. A fully-modeled synchronous generator may be associated with something on the order of two dozen states. This approach has several shortcomings within the context of long-term dynamics.

- The concept of inertia is not applicable, or can only be applied in an abstract sense, for converter-coupled generating stations.
- The models associated with transient stability studies are not accurate for the study of longer-term dynamics.
- The library of standard models appropriate for the study of longer-term dynamics is missing or inadequate within traditional transient stability toolsets.
- Using the transient stability approach for the study of longer-term dynamics requires the user to carry forward, and integrate, many states that are not applicable to the intended outcome of the study.

Even at the onset of microprocessor-based AGC power engineers had begun to think about ways to study long-term dynamics outside the framework of transient stability simulations. In 1976, Taylor and Cresap proposed aggregating all inertia dynamics into a single swing equation that could be used to estimate system frequency, and from which all system governor and AGC algorithms could derive ([25], [26]). Additional work on study methods for AGC and frequency response issues continues through the present day ([21], [29], [16]).

The adaptive modeling approach proposed herein builds upon the previous work without discarding the transient stability framework. The primary goal of the approach is to improve simulation accuracy by introducing models *appropriate for the simulation time step* at the appropriate time within a simulation. The following run-time modifications to transient stability simulation are proposed:

1. In a post-contingency state, when oscillatory energy from all synchronous generators in the study case has become sufficiently small, swap the model of the individual generator?s inertia out, and replace it with an aggregated system inertia. The aggregated swing equation will yield an aggregated system frequency, and this frequency will be used as the input for all governor and AGC response.
2. In a post-contingency state, when exciter states have settled sufficiently, swap all exciter models out and replace them with a constant bus voltage magnitude in the network model unless the generating station is VAR-limited.
3. In a post-contingency state, when governor states have settled sufficiently, swap all full-order governor models out and replace them with simplified PI governor models followed by simplified turbine models thereby significantly reducing the order of governor equations.
4. Add simplified Over-Excitation Current Limiter (OECL) models at appropriate generating stations to improve realism of models related to VAR management.
5. Add flexible timer models and apply them to tap changing transformers and shunt capacitors to improve realism of models related to VAR management.
6. Add AGC models.

Figure 7.3 shows a signal flow diagram appropriate for simulation of slow dynamics. The proposed overall simulation framework begins with a traditional transient stability case incorporating models appropriate for simulation time steps on the order of 10 milliseconds. A contingency is established, and traditional methods described elsewhere in this report are used to study transient and small-signal stability aspects related to the contingency. When oscillatory transients have quieted we adapt the models so that they are suitable for moving to a time step on the order of 1 to 2 seconds. Note that we are considering two orders of magnitude increase in the time step.

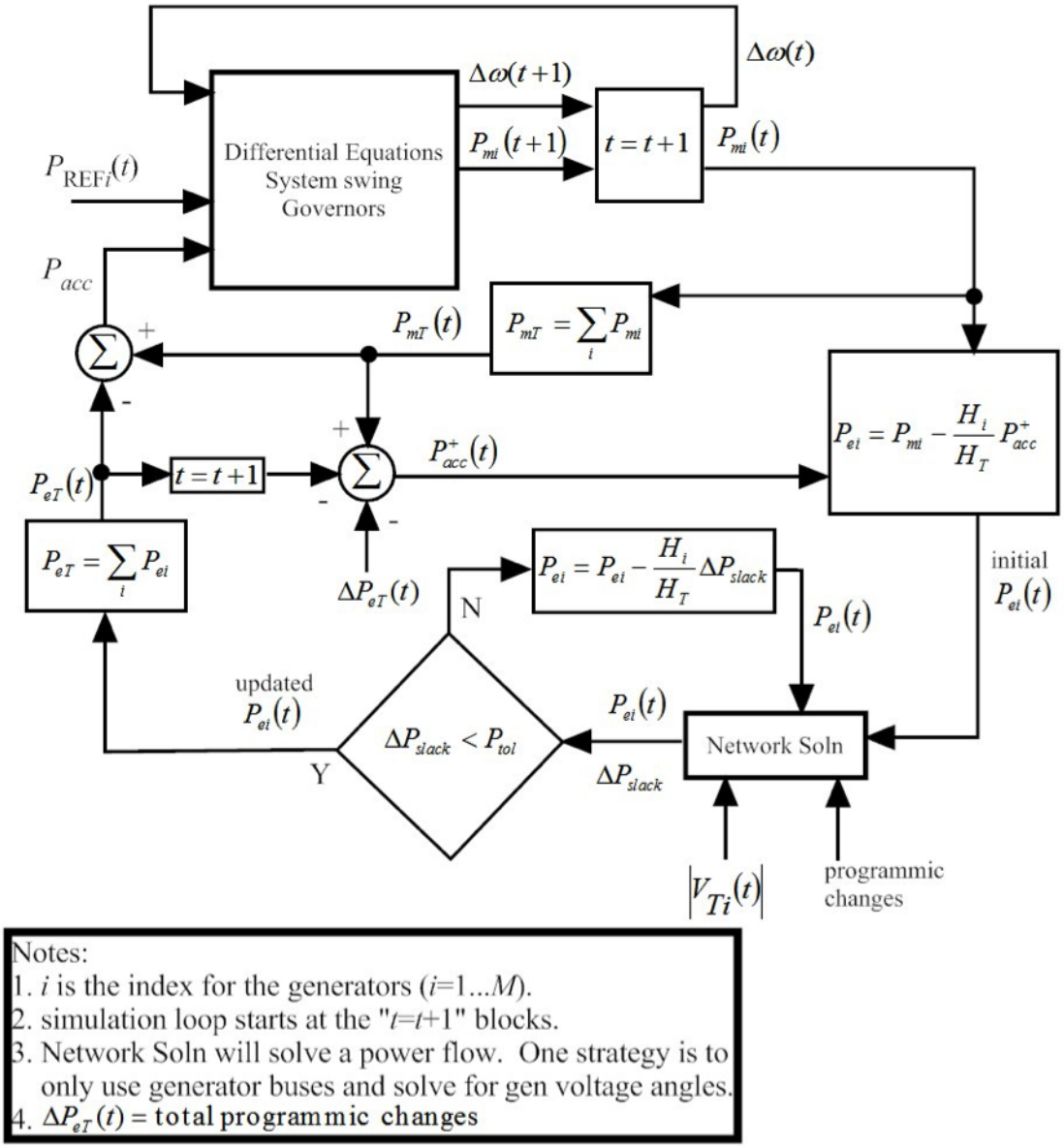

Figure 7.3. Signal flow diagram for slow dynamics simulation framework.

This work promises to greatly enhance the capabilities of simulating high penetration PV sce-

narios by improving our ability to model and simulate longer-term dynamics. The primary issues associated with high penetration scenarios may not lie with electro-mechanical interactions, but may instead lie with our ability to effectively redispatch generation dynamically. The new simulation framework offers to provide the engineering community with the tools to study these effects.

This page intentionally left blank.

Chapter 8

Time-domain simulation results with high PV penetrations

Previously, we utilized PST's linearization capabilities to estimate system eigenvalues and identify various modes present in example power systems. In order to measure the prevalence of each mode, particularly the interarea and local modes, we sought to excite each test system and examine its time domain response to various perturbations. This allowed us to corroborate the time domain responses with the system modes as viewed from the frequency domain. By looking at specific time domain responses such as machine speed differences, we were able to identify interarea and local modes and map them to system eigenvalues identified in the stiffness analysis. As in the stiffness analysis, we focused on examining the smaller KRK system and the larger mini-WECC system.

8.1 Signal processing architecture

In order to perform mode identification of time domain signals, we developed a specific signal processing architecture. The general structure of our time domain simulations began with a few seconds of steady state to initialize the numerical integrators and proceeded with some type of perturbation to excite system modes, e.g., a three-phase fault or generation drop. In these time domain simulations, we used a fixed step size of a quarter cycle corresponding to a sampling frequency of 240 Hz.

The signal processing architecture developed is summarized in Figure 8.1. Since we are primarily interested in the system response to a perturbation, we first crop the signal of interest to ignore the steady state and very beginning of the perturbation response. In the case of a three-phase fault simulation, we do this to approximate isolating the impulse response of the system. Since the power system dynamics we are interested in tend to occur in the 6 Hz or slower regime, it is unnecessary to perform a frequency domain transformation on the entire signal. For easier analysis, we implemented a downsampling routine to remove superfluous signal samples. We pass the cropped signal through an anti-aliasing filter whose nominal cutoff frequency is 6 Hz. This anti-aliasing filter is implemented as a third-order Butterworth low pass filter (c.f. Figure 8.2) which was selected because of its maximally flat passband and smooth rolloff past the cutoff frequency [3]. Following this filtering, we downsampled the resulting signal by a factor of M which was tuned to comply

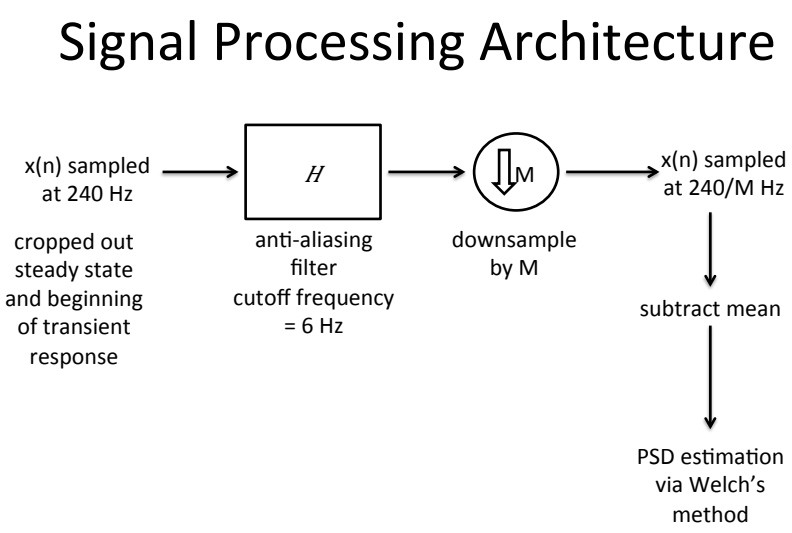

Figure 8.1. Signal processing architecture summary.

with the Shannon-Nyquist reconstruction condition in addition to an engineering safety factor, γ:

$$M = \frac{1}{\gamma}\frac{1}{2}\frac{f_s}{f_c} \tag{8.1.1}$$

where $\gamma = 10$, $f_s =$ the sampling frequency, 240 Hz, and $f_c =$ the cutoff frequency, 6 Hz. The resulting signal is effectively sampled at 240/M Hz. Since we are focused on analyzing oscillatory behavior, we subtract the mean of the signal to produce a zero-mean signal.

To preserve spectral features and limit undesirable noise such as spectral leakage from side-lobes attributed to transforming finite duration signals, we applied a signal window to the zero-mean signal before passing it to a power spectral density (PSD) estimation routine. We found that a periodic Blackman windowing signal (c.f. Figure 8.2) produces the clearest PSD estimates due to its compatibility with discrete Fourier transformations [18]. Finally, we used Welch's method for PSD estimation due to its noise reduction properties [31]. Overall, in comparison to a standard FFT procedure without any additional processing, this signal processing architecture is able to produce much clearer spectral peaks which is a boon for corroborating with the stiffness analysis results.

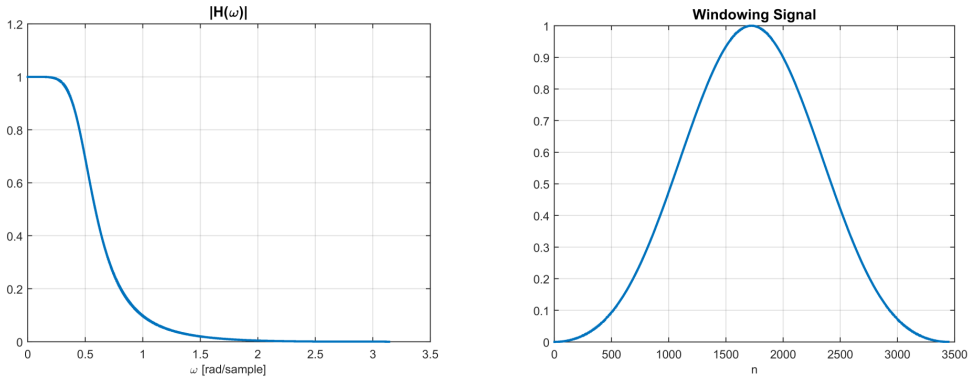

Figure 8.2. Components of signal processing architecture. (left: anti-aliasing filter frequency response magnitude, right: windowing signal)

8.2 KRK system simulations

8.2.1 Three-phase fault with no PV generation

For this simulation, we induced a three-phase fault at Bus 3, in area 1 near the central load of the system. This fault was induced after five seconds of steady state and the total simulation time was 40 seconds.

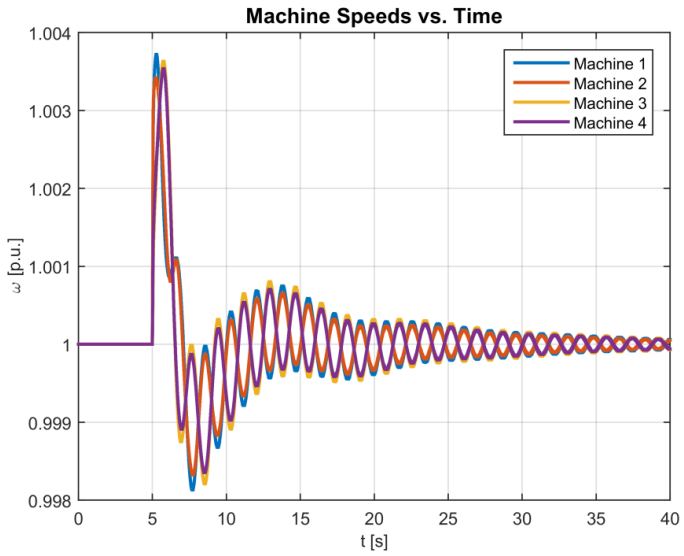

Figure 8.3. Machine speed responses.

Throughout these examples, we examined the machine speed differences between machine 1 and machine 3, which are in different areas, as well as the machine speed differences between machine 1 and machine 2, which are in the same area. This was done to aid in identifying interarea and local modes, respectively.

8.2.2 Local machine speed difference

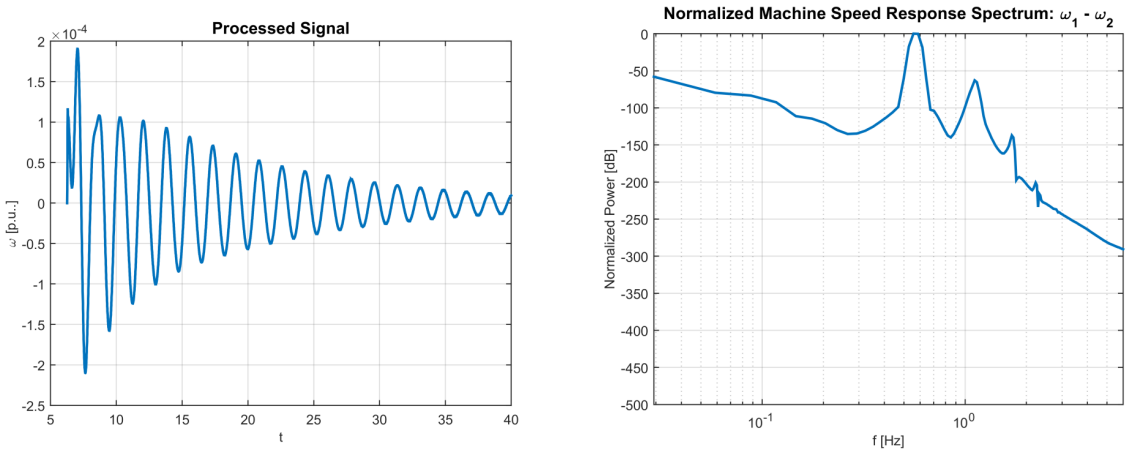

Figure 8.4. Response signal after processing and corresponding estimated spectrum.

The local machine speed difference (c.f. Figure 8.4) doesn't appear to be dominated by a single mode, as evident in the activity of the early response. This indicates there being a non-negligible relatively higher frequency component with a relatively faster rate of decay than the other mode present in the response. This figure displays the estimated power spectral density. It is normalized such that the maximum power indicated is 0 dB. The identified peaks in this spectrum are at 0.571 Hz and 1.113 Hz although the latter may simply be a harmonic of 0.571 Hz. These modes can be readily matched to modes identified from the stiffness analysis.

8.2.3 Interarea machine speed difference

The response signal in this case appears to be dominated by a single mode evidenced by the smooth decay envelope (c.f. Figure 8.5). Using a rough estimation method which assumes a single mode, the time constant of the envelope was estimated to be approximately $0.0816s^{-1}$. The estimated PSD identifies the highest energy frequency to be approximately 0.571 Hz. This matches an identified mode at (-0.07928, 0.571) in the (s^{-1}, Hz) plane.

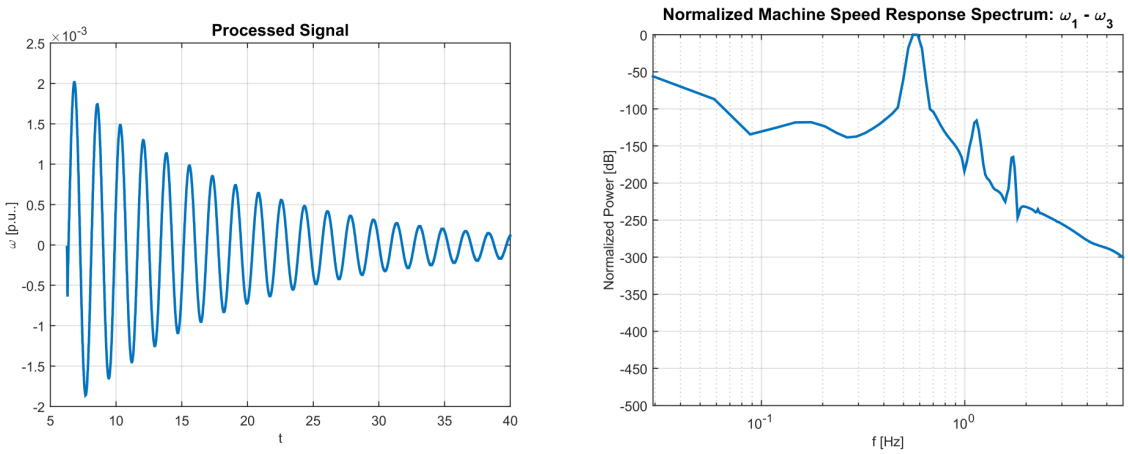

Figure 8.5. Response signal after processing and corresponding estimated spectrum.

8.2.4 Three-phase fault with 50% PV generation

In this example, PV generation was co-located with G2, G3, and G4. Like in previous examples, 50% PV generation indicates that 50% of the active power generated from each synchronous/PV generation pair comes from PV and the rest comes from the synchronous machine; additionally, the synchronous machine has 50% of its original MVA base and, consequently, 50% of its original inertia.

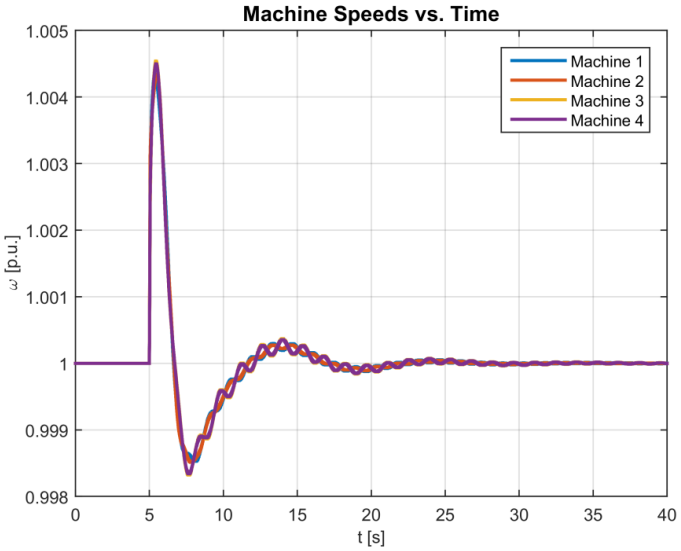

Figure 8.6. Machine speed responses.

8.2.5 Local machine speed difference

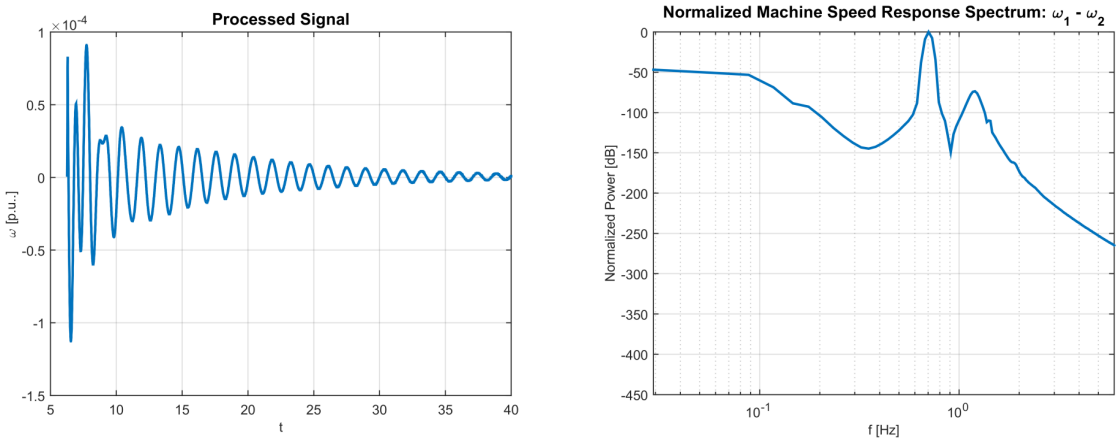

Figure 8.7. Response signal after processing and corresponding estimated spectrum.

In this example, we can observe significant contributions from other mode(s) at the beginning of the disturbance response. The identified peaks in the spectrum are at 0.703 Hz and 1.201 Hz with the latter not being attributable to being a harmonic. The former peak can be matched to an identified mode at ($-0.09358s^{-1}$, 0.7044 Hz). The other peak can be matched to an identified mode at ($-0.785s^{-1}$, 1.194 Hz]. By examining the mode shape of this particular mode (c.f. Figure 8.8), we can verify that this identified peak is indeed a local mode.

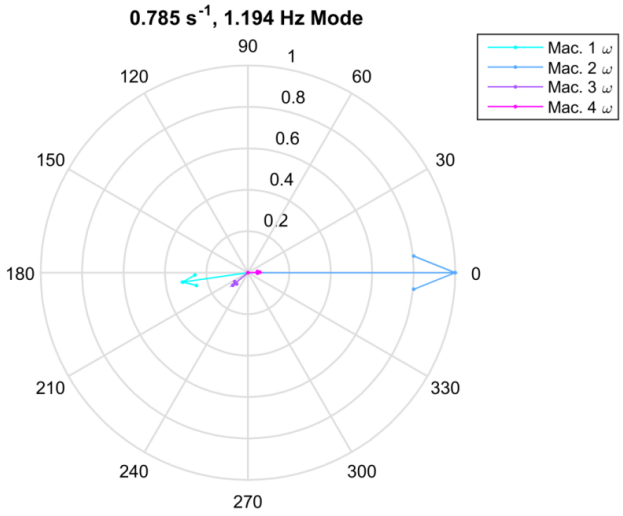

Figure 8.8. Compass plot illustrating mode shape of the identified local mode.

8.2.6 Interarea machine speed difference

There appears to be some more transient activity towards the beginning of the response but it otherwise appears to be dominated by a single mode. Using the aforementioned estimation technique, the time constant of the decay envelope was estimated to be approximately $0.0942s^{-1}$. The identified peak from the estimated spectrum is at 0.703 Hz; this matches the mode to the estimated system eigenvalue at ($-0.09358s^{-1}$, 0.7044 Hz) which we can readily label as the interarea mode based on our previous examples.

8.2.7 Unit decommitment example

Regarding previous analysis involving sweeps across increasing PV generation, it is probable that the concept of unit decommitment needs to be considered. Previously, we demonstrated (typically) smooth and continuous behavior in system stiffness as a function of solar fraction. In practice, it is more likely that synchronous machines are decommitted when solar generation percentage exceeds particular thresholds for, e.g., economic reasons. As a result of synchronous machines being decommitted, system modes should likewise disappear altogether. We sought to demonstrate this through an example.

Using the KRK system, we included PV generation co-located with G3 and G4, i.e., in area 2 only. Additionally, we set the exciter transducer time constants associated with G3 and G4 to half that of those associated with G1 and G2. The hypothesis was that this would separate the

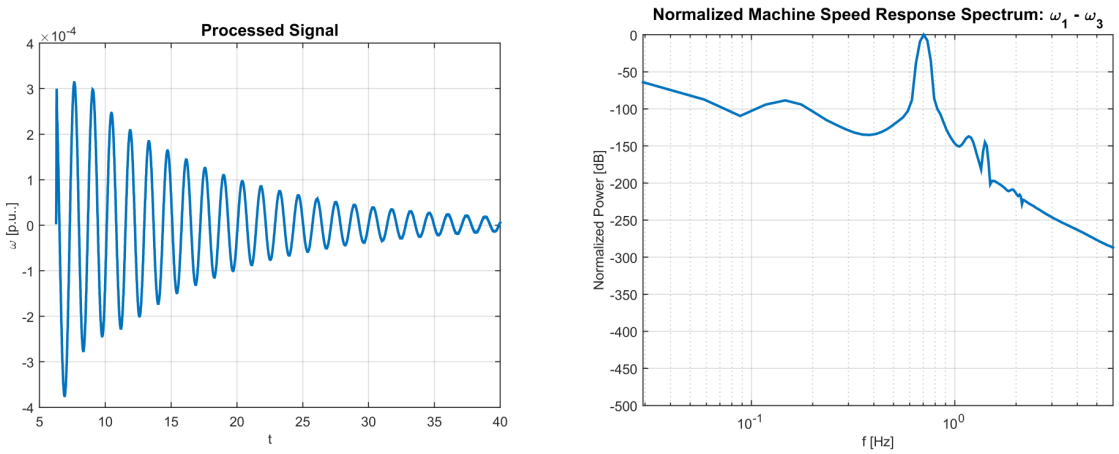

Figure 8.9. Response signal after processing and corresponding estimated spectrum.

modes associated with the exciters in each area so that it would be easier to observe the effects of decommitment. When the solar fraction reaches or exceeds a pre-determined level (set to 50% for this example), the synchronous machines co-located with PV generation are removed from the system and any subsequent time or frequency-domain simulation or analysis is done with this new configuration. Additionally, all generation attributed to decommitted generators is shifted to their co-located PV generation.

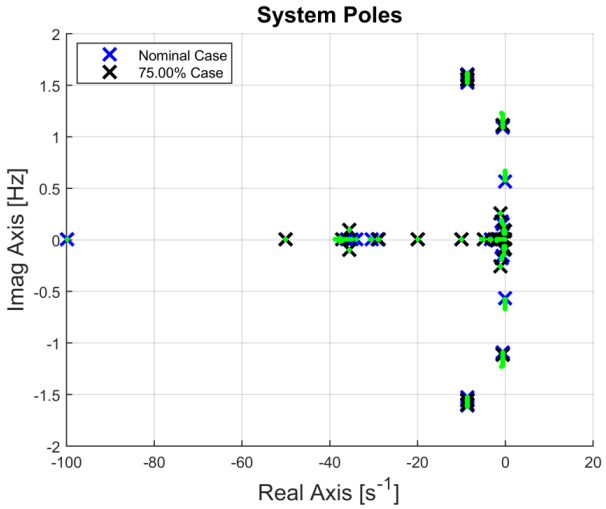

Figure 8.10. System eigenvalue map for a solar fraction sweep with unit decommitment considered.

The most telling indication of decommitment is to see what happens with the fastest decaying modes in the system. As demonstrated before, these eigenvalues associated with the exciters are

typically invariant with respect to solar penetration. Because of decommitment, the eigenvalues present at approximately $100s^{-1}$ are no longer present when the solar fraction value exceeds 50%; this is most evident by the black crosses indicating the 75% solar fraction case being absent at -100 but present at -50. (Note that the exciters associated with the machines that remain committed have double the time constant compared to the exciters of the decommitted machines.) Due to the reduction of the maximum real part of the eigenvalues resulting from decommitment, the stiffness ratio of the system experiences a discrete reduction at 50% solar fraction (c.f. Figure 8.10).

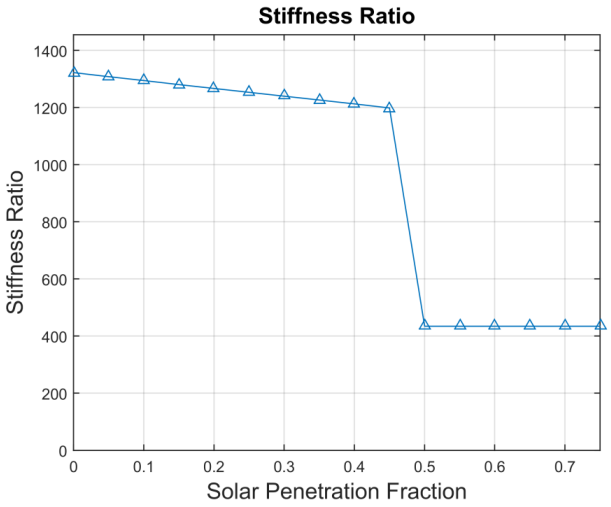

Figure 8.11. There is a discrete jump in the stiffness ratio due to unit decommitment.

One side effect of unit decommitment is the disappearance of the interarea mode. Due to how the example was set up, the synchronous machines that were to be decommitted all reside in area 2. As a result, when decommitment occurs, the only synchronous machines in the system reside in area 1. We can illustrate the effects of this by performing the same three-phase fault experiment using a system that has enacted decommitment.

Figure 8.12 compares the area 1 machine speed difference response to a fault when unit decommitment is or is not considered. Notably, the response is more damped when unit decommitment is enacted. Comparing the two traces, we qualitatively see that when all synchronous machines are present, the response is dominated by a lower frequency, slower decaying mode. On the other hand, when decommitment occurs, the response is dominated by a higher frequency, faster decaying mode. This phenomenon can be explained by comparing the response spectra in each case, shown in Figure 8.13.

Previously, we identified the interarea mode at this solar penetration level to be approximately 0.703 Hz. As we can see in the case of having decommitment, this mode is conspicuously absent. We can attribute this to the lack of synchronous machines in area 2 for those in area 1 to oscillate against.

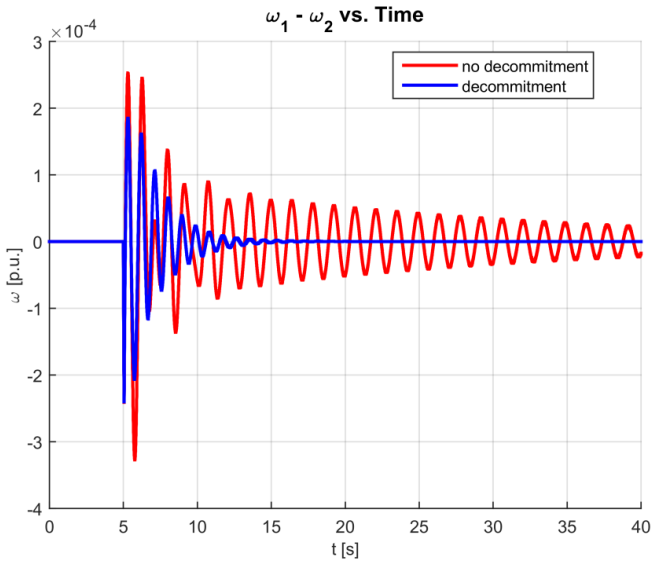

Figure 8.12. Disturbance response signals (local machine speed difference).

8.2.8 Active power generation drop

One transient event of interest to simulate is the sudden increase or decrease in power output of a generator, sometimes called a "generation drop." This is representative of the outage of a single generator among an aggregate collection at a single location. In order to simulate this type of event, we split the active power generation of a representative generator between two identical machines sharing the same point of interconnection to the rest of the system. To simulate the drop in generation, a loss of line (with no fault) event was induced at a particular time, causing a fraction of active power generation at particular location to be disconnected from the rest of the system.

Modifying the KRK system, we included PV generation at G2 and G4. At G3, we split the total active power generation into two identical machines with an 80%/20% split between the two; the total inertia of the pair was split into the same proportions. Both machines were connected to bus 110 with identical lines. To simulate the generation drop, the loss of line event was induced at the line connecting the 20% share machine to bus 110.

We sought to examine the effect of PV penetration levels on the system's responses to this type of event. The response signal of interest was the average machine speed as a function of time. Key features of the response curves include the frequency nadir as well as the steady state settling frequency. The responses are shown in Figure 8.14.

In order to examine the relative trends of the response curve features, we applied a moving average filter to each response signal in order to smooth out high frequency content. While this had an apparent effect on the nadir frequency, it did not change the relation among the different

Figure 8.13. Comparing response spectra for two different scenarios. The dominant peak for each is indicated below each spectrum.

response signals. The resulting signals are shown in Figure 8.15.

The response curve characteristics are summarized in the table below. In general, increasing PV penetration delayed the nadir and decreased its frequency and also decreased the steady state frequency. These effects can be attributed to the reduction of inertia in the system.

Table 8.1. KRK generation drop machine speed response summary.

PV%	Nadir Time [s]	Nadir Speed [p.u.]	Steady State Speed [p.u.]
0%	10.06	0.9966	0.9985
25%	10.07	0.9961	0.9982
50%	10.29	0.9952	0.9979
75%	10.36	0.9942	0.9974

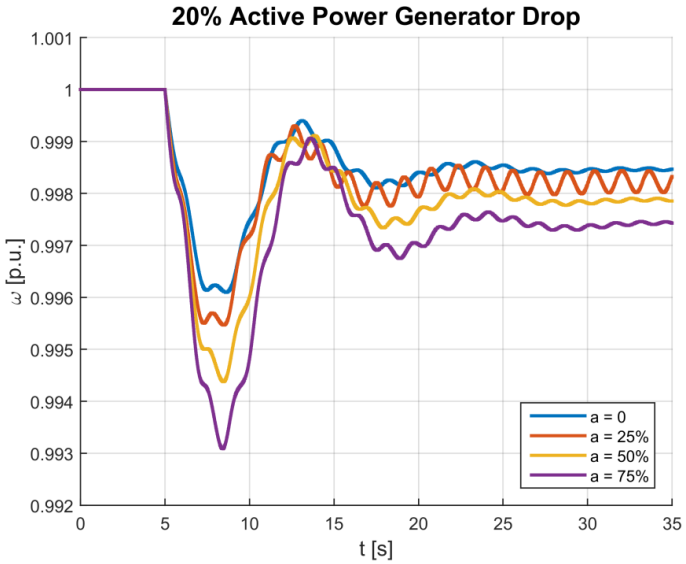

Figure 8.14. Unfiltered mean machine speed over the four machines in the system.

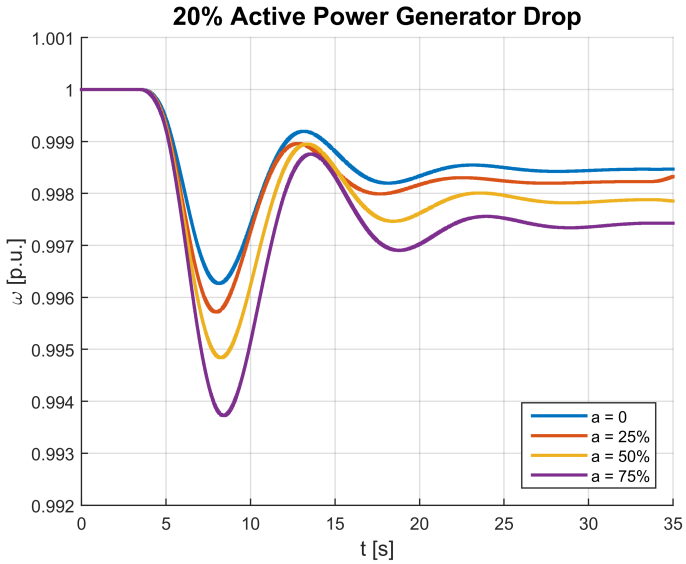

Figure 8.15. Filtered mean machine speed over the four machines in the system.

8.3 miniWECC system simulations

As in the KRK system simulations, we sought to verify that the modes estimated through PST's linearization routine would be present in transient event response simulations for the miniWECC

case. To do so, we simulated three-phase faults and analyzed machine speed difference signals using our signal processing architecture to estimate the spectra of the responses. Relevant machines were selected based on the mode shapes that we identified during the stiffness analysis. For example, for North-South Mode A, the Alberta and Arizona machine speeds were the most out of phase out of all machine speeds based on the estimated mode shape. Therefore, in order to try to identify North-South Mode A through these fault simulations, we used the machine speed difference between Alberta and Arizona as the signal for processing.

8.3.1 North-South Mode A

As mentioned, North-South Mode A was identified using the machine speed difference signal between Alberta and Arizona. In Figure 8.16, the resulting estimated spectra for the base case and the case with 50% PV are shown. Compared to the KRK system analysis, the spectra for these responses tend to have more identifiable peaks in frequency. For the base case, the dominant frequency was found to be 0.2197 Hz and for the 50% PV case, it was found to be 0.3076 Hz. From the stiffness analysis, these were estimated to be 0.219 Hz and 0.302 Hz, respectively. Slight differences in identified mode frequencies could be attributed to the inherent tradeoff of using Welch's method for power spectral density estimation; noise reduction is gained at the cost of frequency resolution when using the method.

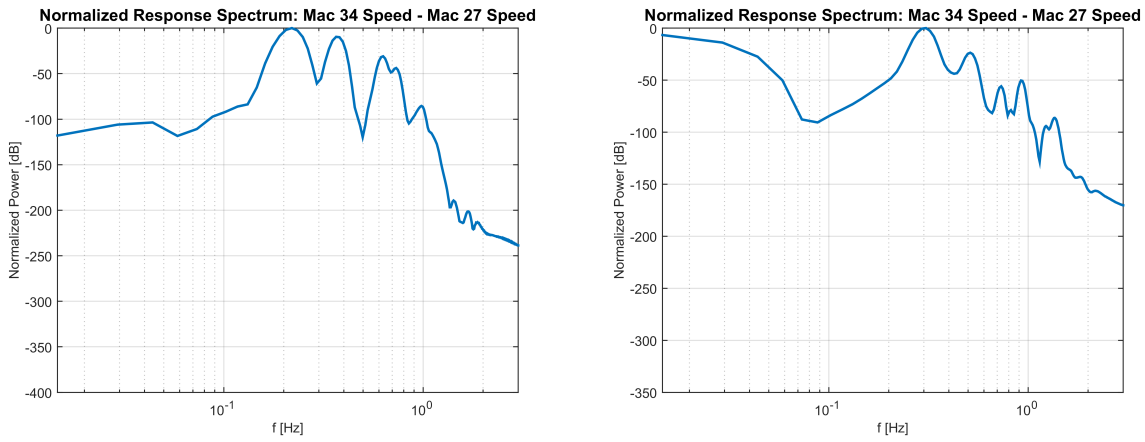

Figure 8.16. Estimated spectra for identifying North-South Mode A. (left: base case, right: 50% PV)

8.3.2 North-South Mode B

To identify North-South Mode B, we looked at the machine speed difference between Alberta and BC. In Figure 8.17, we compare the spectra from the base case and the 50% PV case. For the base

case, the dominant frequency was found to be 0.3662 Hz while for the 50% PV case, it was found to be 0.5127 Hz. These frequencies were estimated to be 0.372 Hz and 0.517 Hz, respectively, from the linearization process. Once again, we found that the frequencies determined through both processes agree closely.

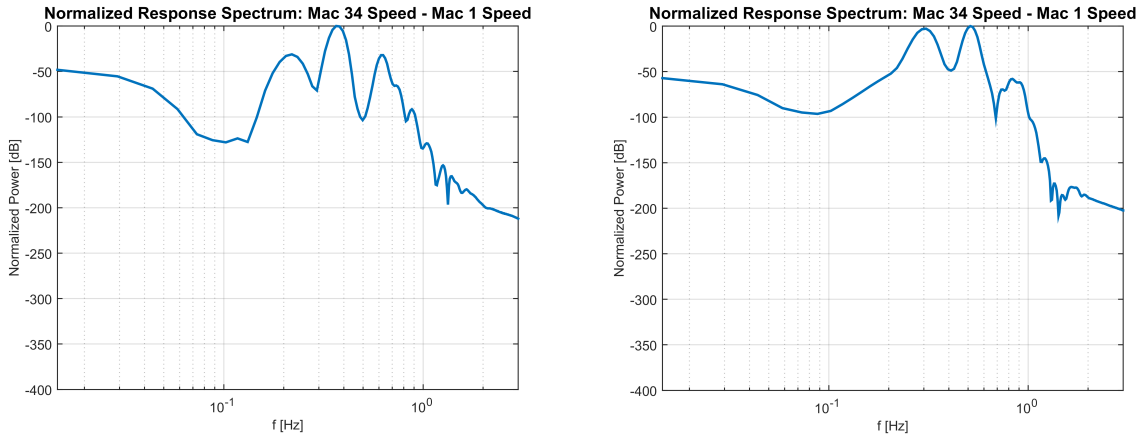

Figure 8.17. Estimated spectra for identifying North-South Mode B. (left: base case, right: 50% PV)

8.3.3 Palo Verde drop simulations

One of the common events that are simulated for the system described by the miniWECC case is known as the "Palo Verde drop." One of the buses in the miniWECC case represents the Palo Verde Nuclear Generating Station, the largest power plant in the United States in terms of net generation, which is located in Arizona. It consists of three reactors which, aggregated, provide 12.3 p.u. active power on a 100 MVA base each in the miniWECC system. In the Palo Verde drop simulations, we simulate the loss of one or two of these reactors, similarly to the active power generation drop simulations in the KRK system. Likewise, we use the mean machine response to analyze how increased PV penetration affects the entire system's behavior in response to these events. As in the previous generation drop simulations, increased PV% results in deeper nadirs, slower settling times, and lower steady state machine speeds, all of which are behavior characteristic of reductions in inertia. Furthermore, these behaviors are exacerbated when more generation is dropped, e.g., double Palo Verde drop compared to single drop.

8.4 Summary

The objective of these time domain simulations was twofold. We sought to validate the results of Section 4 by corroborating the modes estimated through eigenanalysis with those that could be

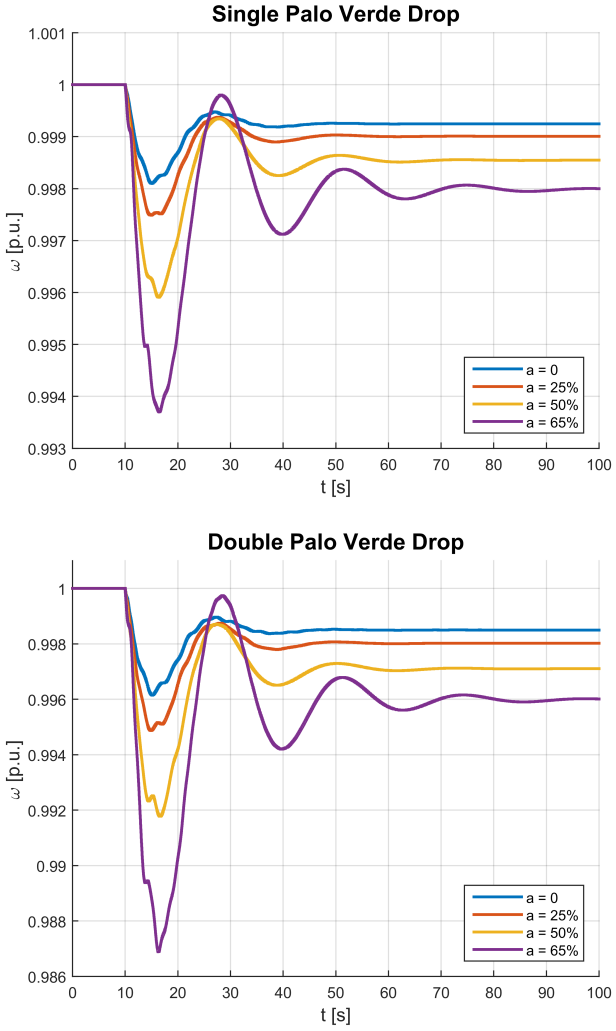

Figure 8.18. Mean machine speed response to Palo Verde drops.

excited through small perturbations of the system. We also sought to analyze dynamic behavior of systems in response to disturbances and how this behavior would be affected by increased photovoltaic penetration. We were able to accurately match modes estimated in Section 4 by simulating three-phase faults and applying our signal processing architecture to estimate the power spectral density of the resulting responses. Although we already determined that system stiffness is not a sufficient indicator of the requirements for numerically simulating a power system, we demonstrated that it is important to consider external factors such as unit decommitment when increasing PV penetration when performing simulations; such factors may affect, for example, the range of dynamics that need to be simulated (e.g., by removing the fastest modes) and/or change system response behavior entirely (e.g., the disappearance of interarea modes). Trends observed in our simulations include increased decay rates of modes (but not necessarily increased damping) with increased PV penetration as well as deeper machine speed nadirs and lowered steady state machine speeds in generation drop events.

This page intentionally left blank.

Chapter 9

Loose ends

In this study, we primarily focused on improving the viability of dynamic simulations as described in the report's title from the perspective of modifying the numerical integration schemes that are used. In Section 6, we addressed the path of considering variable time step integration methods which are sparingly used today. In Section 7, we addressed the limitations of how simulations are conducted today and the gaps in simulation capabilities that inhibit the integration of large amounts of PV generation from a modeling deficit perspective. In addition to the slow dynamics mentioned in that section, others need to be considered, including prime mover effects, state of charge tracking for energy storage systems, wind speed variations, and solar irradiance variations. These dynamics, which play out over time frames of several minutes, are typically neglected due to most simulations being limited to about 60 seconds in duration.

We presented our analysis at various WECC Renewable Energy Modeling Task Force (REMTF) meetings over the course of the project and received feedback from stakeholders and vendors. In addition to the slow system dynamics modeling gaps addressed in Section 7, attention was also given to the fast system dynamics that are typically not modeled in positive sequence modeling environments. Such dynamics include those of the phase locked loop (PLL) systems used for frequency and phase detection and the inner current regulators, both of which have dynamics well into the kilohertz range. One idea for improving feasibility of extended term simulations included throwing out faster dynamics to enable the opportunity to, e.g., increase simulation step size. While it is plausible that the effects of such faster dynamics may be negligible for extended term simulations, it does not seem to be a viable solution if we wish to preserve simulation fidelity as much as possible. One other aspect of system modeling that should be considered is to investigate how interconnection impedance for PV power plants is affected as PV penetration level increases. Increased PV penetration levels would cause low short-circuit ratios, a measure of AC system strength, to become a factor. Wind and solar power plants connected to weak grids with low short-circuit ratios are not uncommon and dynamic models developed by the WECC REMTF are not intended for these plants. This issue ties into the common theme of a current gap in modeling capabilities.

Based on feedback from some software vendors, it was discovered that a significant selection of the dynamic models that have been written in some of the dynamic simulation software used today were written in a way that tie them to the second order Adams-Bashforth integration scheme. As a result, it would require a significant overhaul to change these models to be compatible with other integration schemes, such as those analyzed in this study. While this is a valid concern for current software, we still posit that the development of future simulation software and/or updates

to current software should have dynamic models retain the flexibility to be used with any desired integration scheme. This would enable future updates to the software's integrator that could, for example, improve the feasibility of extended-term simulations.

Chapter 10

Conclusion

In this study, we examined several of the paths forward that could help dynamic simulation software perform extended-term simulations of power systems with high penetrations of PV generation. Our primary focus was to look at how we could change the way current simulation software performs numerical integration in order to accommodate the needs of high PV penetration systems while managing data and computation concerns that arise with extended simulation durations. We used Power Systems Toolbox (PST) in MATLAB as our research and development platform because of the ability to modify its code as needed. We used a current injection model to represent PV power plants and scaled back the inertia of traditional synchronous machines as generation was shifted to the PV power plants.

We used PST's linearization methods to estimate the eigenvalues of several power system test cases. This allowed us to get an idea of the typical layouts of power systems' eigenvalues and determine the numerical integrator's needs from a numerical stability perspective. This drove us to analyze a set of explicit integration schemes, including Heun's method, the second order Adams-Bashforth method, and the fourth order Crane-Klopfenstein method. We evaluated each of these schemes on their computational performance, accuracy performance, and numerical stability. While we decided that CK-4 had the greatest potential for reducing computational burdens while retaining numerical stability for many simulation scenarios, we also showed that Heun's method had the greatest flexibility while possessing the opportunity to increase simulation step sizes because of its relatively large region of absolute stability. In the event that the system to be simulated does not have fast, high frequency modes, CK-4 is most likely able to increase its step size compared to the other integrators that we evaluated.

While the bulk of our analysis focused on analyzing fixed time step, explicit integration schemes, we also considered the possibility of variable time step integration. Such methods also have potential to improve extended term simulation viability due to their ability to adapt the time step as the system dynamics evolve but require finesse and additional logic (error/time step control) to implement.

When considering extended term simulations, especially in the case of high PV penetration systems, we determined that there are various deficits in power system modeling. Dynamics in both the slow and very fast regimes are not modeled in transient and small signal stabilities due to the scope of the systems typically studied as well as the simulation durations that are typically used. Simulations with minute-long durations do not need to consider phenomena that occur over

minutes or hours. Dynamics that are in the kilohertz frequency range are typically negligible in most systems that are simulated. However, all of these dynamics need to be considered when extending the simulation durations and when including large amounts of inertialess PV generation, which behaves significantly differently from conventional synchronous machines.

In conclusion, there are many paths forward to help develop the capability of simulating systems with high PV penetration levels over long time periods. There is room for developing the numerical integration schemes that are used in order to reduce computational and data storage burdens. There are also gaps in power system modeling capabilities that need to be filled, especially for high PV penetration scenarios. Developments in both these regards should pave the way for realistic simulations of systems with high PV penetration over extended durations.

Bibliography

[1] E. H. Abed, D. Lindsay, and W. A. Hashlamoun. On participation factors for linear systems. *Automatica*, 36(10), 2000.

[2] M. Y. Borodulin. Effect of numerical integration on critical time evaluation in power system stability studies. *IEEE Power and Energy Society General Meeting*, 2013.

[3] S. Butterworth. On the theory of filter amplifiers. *Wireless Engineer*, 7(6), 1930.

[4] J. H. Chow and K. W. Cheung. A toolbox for power system dynamics and control engineering education and research. *IEEE Transactions on Power Systems*, 7(4):1559–1564, November 1992.

[5] R. L. Crane and R. W. Klopfenstein. A predictor-corrector algorithm with an increased range of absolute stability. *J. ACM*, 12(2):227–241, April 1965.

[6] B. Ehle. High order a-stable methods for the numerical solution of systems of d.e.'s. Technical report, University of Waterloo, 1968.

[7] R. Elliott, P. Pourbeik, and J.J. Sanchez-Gasca. Generic photovoltaic system models for wecc. *IEEE Power and Energy Society General Meeting*, 2015.

[8] A. Ellis, B. Karlson, and J. Williams. Utility-scale photovoltaic procedures and interconnection requirements. Technical report, Sandia National Laboratories, February 2012.

[9] WECC Renewable Energy Modeling Task Force. Wecc pv power plant dynamic modeling guide. Technical report, Western Electricity Coordinating Council, April 2014.

[10] C. Fu. High-speed extended-term time-domain simulation for online cascading analysis of power systems. Technical report, Iowa State University, 2011.

[11] C. Fu, J.D. McCalley, and J. Tong. A numerical solver design for extended-term time-domain simulation. *IEEE Transactions on Power Systems*, 2013.

[12] IEEE SCC21 Work Group. Ieee std 1457 standard for interconnecting distributed resources with electric power systems.

[13] W.D. Humpage and B. Stott. Predictor-corrector methods of numerical integration in digital-computer analyses of power-system transient stability. *Institution of Electrical Engineers Proceedings*, 112, 1965.

[14] H. Illian. Frequency control performance measurement and requirements. Technical report, Lawrence Berkeley National Laboratory, 2010.

[15] M. Klein, G. J. Rogers, and P. Kundur. A fundamental study of inter-area oscillations in power systems. *IEEE Transacations on Power Systems*, 6, 1991.

[16] M. Lotfalian, R.Schlueter, D. Idizior, P. Rusche, S. Tedeschi, L. Shu, and A. Yazdankhah. Inertial, governor, and agc/economic dispatch load flow simulations of loss of generation contingencies. *IEEE Transactions on Power Apparatus and Systems*, PAS-104(11), 1985.

[17] O. Nevanlinna and A.H. Sipila. A nonexistence theorem for explicit a-stable methods. *Mathematics of Computation*, 28, 1974.

[18] A. Nuttall. Some windows with very good sidelobe behavior. *IEEE Transactions on Acoustics, Speech and Signal Processing*, 29, February 1981.

[19] Reactive Reserve Working Group (RRWG) of the Western Electricity Coordinating Council. Guide to wecc/nerc planning standards i.d: Voltage support and reactive power. Technical report, WECC, March 2006.

[20] WECC Renewable Energy Modeling Task Force of the Western Electricity Coordinating Council. Wecc guide for representation of photovoltaic systems in large-scale load flow simulations. Technical report, Western Electricity Coordinating Council, August 2010.

[21] D. Prowse. Improvements to a standard automatic generation control filter algorithm. *IEEE Transactions on Power Systems*, 8(3), 1993.

[22] S. Ranganath and R. J. Clifton. A second-order accurate difference method for systems of hyperbolic partial differential equations. *Computer Methods in Applied Mechanics and Engineering*, 1972.

[23] J.J. Sanchez-Gasca, R. D'Aquila, W.W. Price, and J.J. Paserba. Variable time step, implicit integration for extended-term power system dynamic simulation. *Power Industry Computer Application Conference*, 1995.

[24] B. Stott. Power system dynamic response calculations. *Proceedings of the IEEE*, 1979.

[25] C. Taylor and R. Cresap. Real-time power system simulation for automatic generation control. *IEEE Transactions On Power Apparatus and Systems*, 1976.

[26] C. Taylor, K. Lee, and D. Dave. Automatic generation control analysis with governor deadband effects. *IEEE Transactions on Power Apparatus and Systems*, 1979.

[27] D. Trudnowski. Properties of the dominant inter-area modes in the wecc interconnect. https://www.wecc.biz/Reliability/WECCmodesPaper130113Trudnowski.pdf, January 2012.

[28] D. Trudnowski, D. Kosterev, and J. Undrill. Pdci damping control analysis for the western north american power system. *Proceedings of the IEEE Power and Energy Society General Meeting*, 2013.

[29] L. Wang and D. Chen. Automatic generation control (agc) dynamic simulation in pss®e.

[30] G. Wanner. Dahlquist's classical papers on stability theory. *BIT Numerical Mathematics*, 46, 2006.

[31] P. D. Welch. The use of fast fourier transformfor the estimation of power spectra: A method based on time aver. aging over short, modified periodograms. *IEEE Transactions on Audio and Electroacoustics*, AU-15(2), June 1967.

DISTRIBUTION:

1 Guohui Yuan, Ph.D.
DOE Solar Program SunShot Initiative
U.S. Dept. of Energy
Washington, DC 20585

1 Matt Donnelly
Electrical Engineering
Montana Tech
Butte, MT 59701

1 Juan Sanchez-Gasca
Energy Consulting
GE Energy
Schenectady, NY 12345

1	MS 0576	Raymond H. Byrne	5521
1	MS 1033	Abraham Ellis	6112
1	MS 1033	Shannon Boynton	10661
1	MS 1104	Charles J. Hanley	6110
1	MS 1140	Ricky Concepcion	6113
1	MS 1140	Ryan Elliott	6113
1	MS 1140	Ross Guttromson	6113
1	MS 0899	Technical Library	9536 (electronic copy)


Sandia National Laboratories